NIST Technical Note 2100

Measurements and Modeling of Spherical CH_2F_2-Air Flames

Michael J. Hegetschweiler
John L. Pagliaro
Lukas Berger
Raik Hesse
Joachim Beeckmann
Heinz Pitsch
Gregory T. Linteris

This publication is available free of charge from:
https://doi.org/10.6028/NIST.TN.2100

National Institute of Standards and Technology
U.S. Department of Commerce

NIST Technical Note 2100

Measurements and Modeling of Spherical CH_2F_2-Air Flames

Michael J. Hegetschweiler
Gregory T. Linteris
Energy and Environment Division
Engineering Laboratory
National Institute of Standards and Technology

John L. Pagliaro
Gexcon

Lukas Berger
Raik Hesse
Joachim Beeckmann
Heinz Pitsch
Institute for Combustion Technology,
RWTH Aachen University, Germany

This publication is available free of charge from:
https://doi.org/10.6028/NIST.TN.2100

July 2020

U.S. Department of Commerce
Wilbur L. Ross, Jr., Secretary

National Institute of Standards and Technology
Walter Copan, NIST Director and Undersecretary of Commerce for Standards and Technology

National Institute of Standards and Technology Technical Note 2100
Natl. Inst. Stand. Technol. Tech. Note 2100, 43 pages (July 2020)
CODEN: NTNOEF

This publication is available free of charge from:
https://doi.org/10.6028/NIST.TN.2100

Abstract

The burning velocity of mixtures of refrigerant R-32 (CH_2F_2) with air over a range of equivalence ratios are studied via spherically expanding flames (SEFs) in a large, optically accessible spherical chamber at constant pressure. Shadowgraph images from a high-speed video camera are analysed to yield flame radius as a function of time. Data reduction techniques are explored and direct numerical simulations of the flames are performed with the FlameMaster code, using detailed kinetics. The flame radius as a function of time is accurately predicted by the simulations. Flame stretch and thermal radiation (using an optically thin model) occur simultaneously and make extraction of the unstretched burning velocity from the experimental data difficult. For these low burning velocity flames, the numerical simulations show that stretch and radiation effects are particularly important, and different data reduction schemes can have large effects on the inferred burning velocity.

Key words

Burning Velocity, Flame Stretch, Laminar Flame Speed, Radiation, Refrigerant Flammability, R-32.

Table of Contents

List of Figures

1. Introduction

Vapor-compression refrigeration and space conditioning devices are widely used. As a result of the Montreal Protocol [1], many of the high ozone-depletion potential (ODP) working fluids, e.g. the chlorofluorocarbons (CFC), have been largely phased out. Their replacements, the hydrofluorocarbons (HFC), have zero ODP, but like their predecessors, have a large global warming potential (GWP). The contribution of the HFCs to the total radiative forcing of the earth is projected to be large, estimated to be about 20% of the total increase in radiative forcing from CO2 between 2012 and 2050 [2]. Alternatives exist but have not been adopted largely because of the absence of codes and standards for their safe use. Unfortunately, some of the approaches adopted to make these compounds more reactive in troposphere, such as using unsaturated hydrofluorocarbons (alkenes) and increasing the hydrogen substitution, also makes them more flammable. Hence, flammability is an additional parameter that the Heating, Ventilation, Air-Conditioning, and Refrigeration (HVAC&R) industry must consider when selecting working fluids (beyond the presently considered thermodynamic, fluid dynamic, heat transfer, GWP, and toxicological properties). To facilitate their safe use, it is essential that industry have data on their combustion properties as well as a test metric to rank their flammability and predict their full-scale behavior.

The unstretched laminar burning velocity S_u^0 is a useful metric for flammability. It is a fundamental combustion parameter containing information related to the mixture's heat release, reactivity, and transport properties, and is used as a scaling parameter for turbulent flame speed [3] and to simulate full-scale explosions [4, 5]. The laminar burning velocity is correlated with lean flame extinction, minimum ignition energy, and flame quenching diameter. Moreover, it is the subject of developing international codes and standards for refrigerant flammability [6, 7].

The refrigerant difluoromethane (R-32, CH_2F_2) is selected for the present study. It is flammable and has an intermediate GWP_{100} value for a refrigerant, 677 [8] as compared to 1924 for R-410A and < 1 for R-1234yf [9]. It is widely used, both as a pure compound in Asia and as component of blends in other countries. R-32 has an intermediate burning velocity relative to other refrigerants, with the currently adopted peak value of $S_u^0 = 6.7$ cm/s at standard conditions. Since its burning velocity is used both as a calibration metric for existing flammability standards [6], and for kinetic mechanism development [10], accurate values of its burning velocity are very important.

Difluoromethane in premixed flames has been studied previously both as a pure fuel and as a flame inhibitor added to hydrocarbon-air flames. For premixed CH_4-Air flames with added CH_2F_2, Linteris and Truett [11] measured (via a nozzle burner) and predicted (via 1-D, planar, adiabatic simulations with the Sandia PREMIX code) the burning velocity reduction caused by the addition of CH_2F_2 and analyzed the effects of CH_2F_2 on the reaction pathways and radical consumption. For flames of pure CH_2F_2 as fuel, Takizawa et. al. [12, 13], Moghaddas et al. [14], Burrell et al. [15], and Burgess et al. [16] used the constant volume combustion method to deduce the burning velocity from the pressure rise, with experiments in both normal gravity [12] and microgravity [13]. Takizawa et al. [13] also used the constant pressure method, employing a 3.9 L cylindrical chamber with Schlieren imaging to deduce the flame speed from the outward propagation speed of the horizontal edges of the flame. Tests were additionally conducted using a 2.9 L cylindrical chamber from which both the pressure rise

and Schlieren image were needed to obtain the burning velocity [12] (due to the slight pressure rise). Jabbour and Clodic [17, 18], Papas et al. [19] and Takizawa et al. [20] used a 4 cm inner diameter vertical tube (closed at the top) and measured the upward flame propagation rate (and its area) to deduce the burning velocity.

Calculations for premixed flames of $CH_2F_2/O_2/N_2$ mixtures have been performed, mostly for one-dimensional, planar, adiabatic conditions. Papas et al. [19] compared predicted burning velocities with vertical tube measurements of their own and of Jabbour [17], as well as with constant volume method measurements of Takizawa et al. [21]. Their simulations were performed using the kinetic mechanism originally developed at NIST for HFC flame inhibition of hydrocarbon-air flames [22, 23], as well as using modified NIST HFC mechanisms with key rates adjusted to match their experimental data. Linteris et al. [24] performed simulations for various C_1 and C_2 HFCs, including CH_2F_2, using a slightly updated NIST HFC flame inhibition mechanism.

In all of the above work, the simulations did not include the effects of stretch and radiation, which have typically been found to be important for slow burning flames [25]. Recently, Burrell et al. [16] and Burgess et al. [10] have presented new experimental data for $CH_2F_2/O_2/N_2$ mixtures, for a range of oxygen mole fraction and equivalence ratios ϕ, in constant volume experiments in which the effects of optically-thin thermal radiation have been included in the data reduction [26]. The 1-D, planar, adiabatic simulations in this work were performed using a newly developed detailed kinetic model for R-32 combustion based on the experimental burning velocity data. Recently, Hegetschweiler et al. [27] have reported experiments and simulations for outwardly propagating spherical flames of R-32 with air, modeled the experiments with a time-dependent, 1-D spherical flame model employing detailed chemistry, and described the role of stretch and radiation for those experiments. The present work expands upon the earlier work [27], presenting data for more values of the fuel-air equivalence ratio ϕ, and providing more detailed description of the analyses.

As described above, various methods have been employed for measuring the burning velocity of R-32/air flames. The present work employs an outwardly propagating spherical flame experiment in a large spherical chamber, so that burning velocity as a function of flame radius at nearly constant pressure is obtained, elucidating the effects of stretch, with minimal effects from confinement. Data are obtained over a range of equivalence ratio and flame radius. The experiments are modeled with a direct numerical simulations (DNS) employing a detailed kinetic model developed previously [10], and the results are compared with the experiments and then used to understand the role of flame stretch and radiation.

The present work is important because industry is using the method of constant pressure, outwardly propagating flames with optical imaging for measuring the burning velocity of refrigerant-air flames with very low burning velocities, and papers have appeared in the literature describing measurements as low as 1.5 cm/s (e.g. R-1234yf/air flames, [28, 29]). Consequently, additional insight into the role of stretch and radiation heat losses for refrigerant-air flames is important. While buoyancy is known to be important for refrigerant-air flames with low burning velocity [28, 30, 31], the present work is limited to conditions at which buoyant distortion is relatively minor. The role of buoyancy in slow-burning flames is being addressed in companion work in which 2-D, time-dependent direct numerical simulations are being performed while allowing for buoyant distortion of the flames [32].

2. Experiment

2.1. Apparatus and Procedure

The experimental arrangement is the same as that used previously [27, 33, 34] and is outlined briefly here for convenience. The system employs a visually accessible 30 L spherical chamber and z-type shadowgraph system for high-speed video recording of the outwardly propagating spherical flames. It is based on the design by Faeth and coworkers [35-38] and Takizawa et al. [12]. Mixtures are prepared in the chamber via the partial pressure method, circulated for 3 min (using a stainless-steel bellows pump) to ensure complete mixing, then given 10 min to settle. The sample reactants are CH_2F_2 (Honeywell, Genetron 32, 99.9% purity) and house compressed air that has been filtered and dried, so that the relative humidity is typically less than 2 % [39]. To initiate combustion, a capacitive discharge system generates a controlled spark with variable energy (in the range of 0.05 mJ to 500 mJ) at the center of the chamber. For each test, the ignition energy is gradually increased until ignition occurs, ensuring that the supplied energy is within an order of magnitude of the minimum ignition energy.

A high-speed camera (1500-2500 frames/s) and shadowgraph system provide images of the spherical flame propagation. Custom-developed image analysis software tracks the flame edge at four positions (typically left/right/up/down) and determines the curvature of the flame front at two of the locations, typically the left and right sides since these are least distorted by buoyancy. More details about the flame front radius extraction is given in section 4.2.1.

The experimental system was validated in a previous work for CH_4- and C_3H_8-air mixtures [33]. Data reduction and zero stretch extrapolations were similar to those in the present work; however, different flame radius ranges of data were used for zero stretch extrapolation in the previous work, and radiation effects were neglected. Pagliaro et al. [33] described an uncertainty estimation for the experimental determination of the burning velocity for the same apparatus. The maximum uncertainty (95 % confidence interval) in the unburned laminar flame speed S_u^0 reported is 13% for methane and propane. However, measurement uncertainty is not the only cause of inaccuracies: buoyancy, radiation, and non-linear stretch effects can cause the inferred value of S_u^0 to differ from that of an idealized configuration, and this may vary with reactants. In the present case with CH_2F_2 as a reactant, those effects have a larger influence on the burning velocity as described below and larger uncertainties are expected.

3. DNS Simulations

3.1. Description

The flames are simulated with the open-source code FlameMaster [40] which can describe various 0-D (e.g., plug flow and stirred reactors) and 1-D flame configurations. FlameMaster solves the mass-, momentum-, energy-, and species conservation equations and assumes ideal gas behavior. In our case the equations are solved in a spherical coordinate system and spherical symmetry is assumed such that all quantities depend on radius and time only. To calculate the species diffusion velocities the Curtiss-Hirschfelder approximation is used with mixture-averaged diffusion coefficients. Kinetic, thermal, and transport properties are

calculated from CHEMKIN-like input. All terms are discretized by upwind- or central differencing schemes, which are of first order in non-uniform grids, and a Newton scheme is applied to advance in time. The computational domain spans the radius range 0 cm < r < 11.43 cm. Zero gradient outflow conditions and a fixed dynamic pressure are applied at r = 11.43cm. At r = 0, symmetry is enforced (no flow). A calculation is initialized by a hot kernel in chemical equilibrium with a radius of 0.5 cm using a hyperbolic tangent flame profile A dynamic grid refinement algorithm redistributes the grid points such that gradients are properly resolved. A grid convergence study showed that a total of 1500 grid points is sufficient and is leading to at least 100 grid points in the flame profile. The time is advanced by an implicit scheme and typically results in 10-5 to 10-6 seconds time step sizes. The FlameMaster code is well-validated and widely used for hydrocarbon flames [41]. Nonetheless, since the fuel and kinetic mechanism are new, a validation study is presented in the next section.

3.2. Code Validation

To obtain the laminar unstretched flame velocity $S_{L,u}^0$ with respect to the unburned mixture, the conditions of planar, 1-D, adiabatic flames are typically used. Hence as a first step, the present simulations with FlameMaster are compared with those of Cantera [42] at the same conditions. Radiation and Soret effects are not considered for this validation and the species transport is modeled with mixture averaged species diffusion. Automatic grid refinement algorithms are applied in both codes and it was verified that the calculated burning velocities are grid-converged (303 overall grid points in FlameMaster and from 150 to 250 grid points, depending on ϕ, in Cantera and at least 100 points in the flame profile in both codes). The mass, momentum, species mass fraction, and energy conservation equations are solved until steady state is reached. The inflow composition is R-32 (CH_2F_2) mixed with dry air ($X_{O_2} = 0.21$, $X_{N_2} = 0.79$, T=298 K, P=101.33 kPa). Fig. 1. shows the calculated $S_{L,u}^0$ as a function of equivalence ratio. As indicated, the agreement is within 3 %.

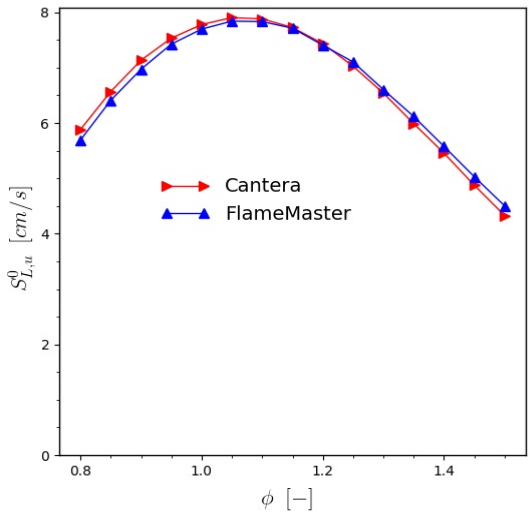

Fig. 1. Calculated laminar, unstretched flame speeds with respect to the unburned mixture by Cantera and FlameMaster (R-32/Air at 101 kPa and 298 K).

3.3. Code Implementation and Data Reduction for 1-D Spherical Flames

3.3.1. Introduction

As a first step to test the consistency of FlameMaster for R-32/air flames, the 1-D planar simulations described above are compared to the unstretched burning velocity obtained from extrapolations of stretched flames to stretched-free conditions. Obtaining unstretched burning velocities from a spherical flame has been well studied; however, it is much more challenging for slow burning flames in which both radiation and flame stretch are important. For the present consistency illustration, however, we assume adiabatic conditions (no radiation). Moreover, in the computations (as opposed to experiments) the flame can be allowed to grow to much larger radii so that flames of low stretch rates are obtained and the zero-stretch extrapolation has smaller uncertainties. The methods of defining the flame location, the extrapolation to zero stretch, and correction for flame contraction due to radiation are described below.

3.3.2. Flame Location

The extraction of the flame front location (flame trace $R_f(t)$) can be done in different ways [43]; 1) following an isothermal surface on the flame temperature profile, 2) following a iso-level of a flame progress variable (e.g. a temperature progress variable $C_T = (T - T_u)/(T_b - T_u)$), or 3) using the peak value location of the fuel consumption rate. Methods 1) and 2) are similar in the case of constant pressure spherical flames since T_b and T_u are constant in time. The iso-level approaches are problematic in that the profile shape changes over time and consequently different flame velocities are obtained depending on the value of the chosen iso-level. It is advantageous to use the peak fuel consumption rate method; however, finding the peak location of a discrete profile with a narrow but most likely poorly resolved peak leads to a noisy flame trace. Therefore, we suggest an alternative method which is simple and features a stable algorithm. The idea is to replace the real flame profile by a step function with constant values in the burned and the unburned regions (i.e., assuming an infinitely thin flame sheet). The flame radius is then calculated by a simple mass balance and reads as

$$R_f = \sqrt[3]{\frac{3\int_0^R Y_f(r)\rho(r)r^2 dr - Y_{f,u}\rho_u R^3}{Y_{f,b}\rho_b - Y_{f,u}\rho_u}} \tag{1}$$

where Y_f is the chosen representative quantity (e.g. fuel mass fraction), ρ the fluid density, R the outer radius of the spherical domain, R_f is the flame front radius, and subscripts u and b indicate states in the unburned and burned region, respectively. All four extraction methods were applied to various R-32/Air flame calculation results and no large differences were observed. This illustrates that the presented integral method is very similar to following the cold tail of the flame (i.e., via tracking a low isotherm, or a low value of an iso-progress variable). Figure 2 depicts the extracted flame front radii in $R_f(t)$ and $S_b(\kappa)$ space.

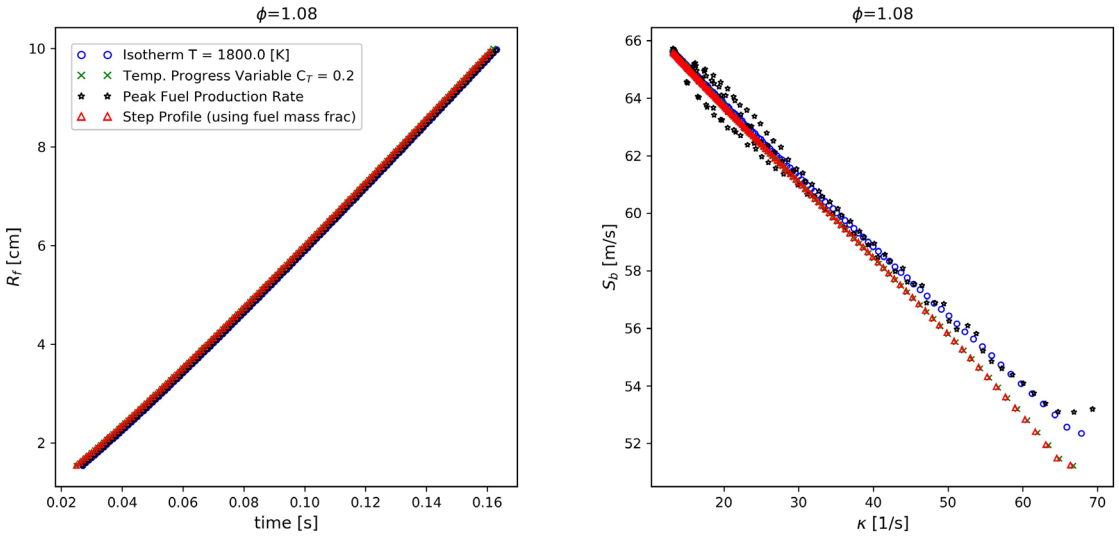

Fig. 2. Flame front evolution traces in flame radius - time (left) and in burning velocity - stretch rate space (right) for an R-32/Air flame, for an equivalence ratio of 1.08 and for different flame location extraction methods.

3.3.3. Stretch Correction

The stretch rate is defined as the relative rate of change of a flame (fluid) surface element and includes, in the case of spherically shaped flames, the effects of fluid strain and curvature. It can be written as

$$\mathrm{K} = \frac{1}{A(t)}\frac{\mathrm{d}A(t)}{\mathrm{d}t} = \frac{2}{R_f(t)}\frac{\mathrm{d}R_f(t)}{\mathrm{d}t} \tag{2}$$

where A is the time dependent area of a surface element and R_f is the flame radius [44]. Stretch has a considerable influence on the flame behavior and depending on the species Lewis numbers (ratio of thermal and mass diffusion) it can increase or decrease the flame velocity. A relationship between flame speed and stretch rate was first proposed by Markstein [45]

$$S_b = S_b^0 - L_b\kappa, \tag{3}$$

in which S_b is the stretched laminar flame speed with respect to the burned mixture, S_b^0 is the corresponding unstretched value and L_b is the burned Markstein length. Note while the laminar burning velocity is usually denoted by $S_{L,b}^0$, we use the notation S_b^0 for the zero stretch laminar flame speed since only laminar flows are considered in this work. Initially this equation was

derived heuristically and later confirmed by asymptotic analysis from first principals under the assumption of weakly stretched flames [46]. It claims a linear dependency of the flame velocity on the stretch rate. A more general model was devised by Kelley et. al. [47] using large activation energy asymptotic and has the form

$$\left(\frac{S_b}{S_b^0}\right)^2 \ln\left(\frac{S_b}{S_b^0}\right)^2 = \frac{2L_b}{S_b^0}\frac{dS_b}{dR_f} - \frac{2L_b\kappa}{S_b^0}. \tag{4}$$

This model was derived under fewer constraints and is valid for positive and negative Lewis numbers, for mixtures of varying stoichiometry, and large stretch rates. This equation is numerically unstable and can lead to non-physical solutions. Kelley et. al. provide a more workable form by expanding Eq. (4) in $1/R_f$ and subsequent time integration, leading to an equation in flame radius and time space. The same can be done for the linear Eq. (3) and the two corresponding relations become

$$R_f + 2L_b \ln R_f = tS_b^0 + C \tag{5}$$

and

$$\mathrm{R_f} + 2\mathrm{L_b}\ln(\mathrm{R_f}) - 4\frac{\mathrm{L_b^2}}{\mathrm{R_f}} - \frac{8}{3}\frac{L_b^3}{R_f^2} = tS_b^0 + C. \tag{6}$$

Equation (5) corresponds to the linear Eq. (3) and Eq. (6) corresponds to the non-linear Eq. (4). These equations can be directly used to fit experimental or calculated $R_f - t$ flame traces. The unstretched burning velocity S_b^0, the Markstein length L_b, and C are fitting parameters and are directly obtained by the fitting process; C is an integration constant satisfying the initial conditions.

3.3.4. Comparisons of Spherical and 1-D Planar Flames

Fig. 3 shows the comparison between flame velocities of planar and spherical calculations, both adiabatic. The maximum deviations occur for higher equivalence ratio but are limited to approximately a 4 % relative difference. As mentioned earlier, theoretically the spherical calculation could run much longer such that zero stretch is approached and the uncertainty would go to zero. Therefore, those 4% error is only valid in this specific case where the largest flame radius was approximately 10 cm, note that the results of both linear and non-linear extrapolations are presented and give results very close to each other for this case.

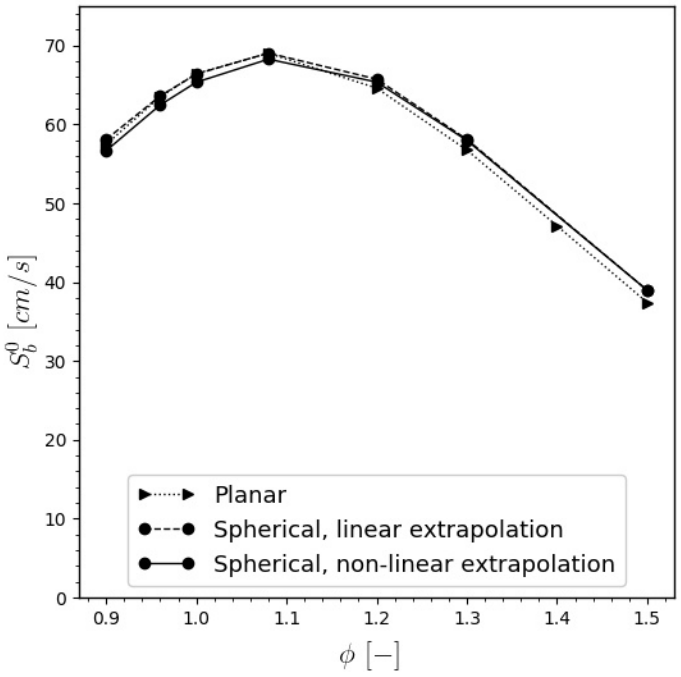

Fig. 3. Comparison of laminar flame speeds (with respect to the burned gas) of one-dimensional planar (stationary, un-stretched) and spherical FlameMaster (unsteady, stretched) calculations. To obtain the zero stretch flame speeds of the spherical calculations linear and non-linear extrapolation for data between radius 1.5 cm and 10 cm are applied.

3.3.5. Radiation: Burned Gas Velocity Correction

Radiation has two important effects on spherically expanding flames, direct (1st order effect) and indirect (2nd order effect). In the direct effect, the hot reaction zone loses energy to the colder surroundings, slowing the chemical reactions and leading to lower burning velocities. The 2nd order effect is due to a continuous cooling of the burned gas behind the flame front, leading to a contraction of the burned gases. This induced contraction velocity invalidates the assumption of quiescent fluid in the burned region. The 1st order influence is included in the raw data of the experiments or calculations (if a radiation model is applied); however, the indirect effect due to burned gas contraction must be accounted for during the post-processing. For fast flames, the assumption of quiescence burned gas is justified (since the contraction velocity is slow relative to the flame propagation rate), but for the present slow burning R-32/air flames, a possible large error on the resulting burning velocity is introduced. For near-limit lean methane-air flames, which have similar flame speeds as the R-32/Air flames, Chen [48] and Yu et al. [49], provide a detailed description of the effect. The correct definition of the burning velocity in this case is

$$S_b = \frac{\mathrm{d}R_f}{\mathrm{d}t} - u_b \tag{7}$$

where u_b is the burned gas velocity. In constant pressure experiments, only $R_f(t)$ (in the laboratory reference frame) is available from the flame images. In calculations however, both R_f and u_b are available such that Eq. (7) can be applied directly to obtain the stretched burning velocity. A problem arises, however, when extrapolations to zero stretch are desired. As described previously, for numerical reasons it is advantageous to use the fitting equations directly for $R_f - t$ space (Eqs. (5) and (6)), not the equations in $S_b - \kappa$ space. Therefore, we propose a burned gas velocity correction which can be directly applied to the extracted flame trace $R_f(t)$ obtained from the simulations. If we denote the observed flame radius as $R_{f,obs}$ and the corrected as $R_{f,corr}$, Eq. (7) can be written as

$$\frac{\mathrm{dR_{f,corr}(t)}}{\mathrm{dt}} = \frac{\mathrm{dR_{f,obs}(t)}}{\mathrm{dt(t)}} - \mathrm{u_b(t)}. \tag{8}$$

Integrating over time from 0 to an arbitrary time *t*, the corrected flame radius trace becomes

$$\mathrm{R_{f,corr}(t)} = \mathrm{R_{f,obs}(t)} - \int_0^{\mathrm{t}} \mathrm{u_b(t')dt'}. \tag{9}$$

The corrected flame trace $R_{f,corr}(t)$ can now be used in Eqs. (5) and (6). Furthermore, the corrected stretched flame speed S_b is simply

$$S_{b,corr} = \frac{\mathrm{d}R_{f,corr}(t)}{\mathrm{d}t}. \tag{10}$$

The effect of the correction on the flame radius history is shown in Fig. 4. To distinguish between the different flame radii and flame velocities we introduce the following notation; $R_{f,ADI}$ for adiabatic quantities, $R_{f,OTM_{obs}}$ and $R_{f,OTM_{corr}}$ denote quantities of calculations with the OTM radiation model without and with burned gas velocity correction, respectively. Note that for adiabatic cases, no distinction must be made between observed and corrected flame radius since the burned gas velocity is always zero. In Fig. 4, the corrected (dark blue line) flame front moves faster than the observed one (orange line), since the burned gas velocity (i.e., contraction) is directed to the center of the flame and the flame speed is underestimated. Similarly, Fig. 5 shows the burning velocity with respect to the burned gases Sb (i.e., the slope of the curves in Fig. 4) using the same notation. The top curve ($S_{b,ADI}$, adiabatic) has the highest burning velocity, while the uncorrected ($S_b = \mathrm{d}R_{f,obs}/\mathrm{d}t$, observed) is the slowest. The curves in the middle of the figure show Sb after correcting for

the burned gas velocity. The difference between $S_{b,ADI}$ and $S_{b,OTM_{corr}}$ is the result of the 1st order radiation effect, whereas the difference between the observed and corrected curves (bottom and middle curves) results from the 2nd order effect.

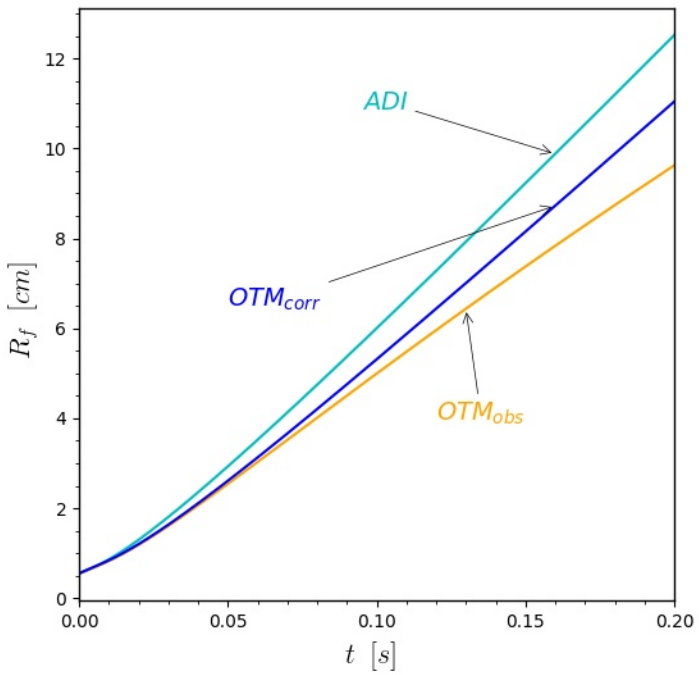

Fig. 4. Flame radius $R_f(t)$ from spherical flame calculation of R-32/Air mixtures, φ=1.08, with and without optically thin radiation (OTM); top curve: calculated $R_f(t)$ for adiabatic conditions, lower curve: observed flame front; middle curve: flame radius which would have occurred with no flame contraction (e.g., corrected via Eq. (9)).

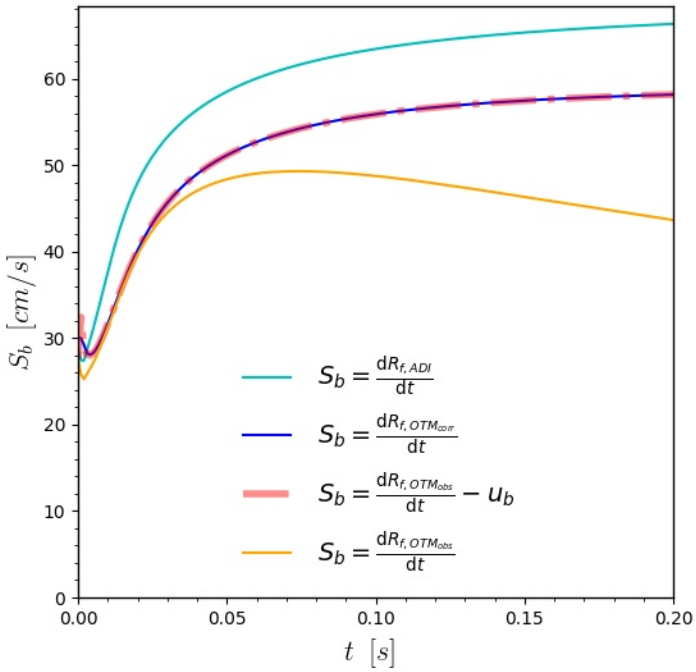

Fig. 5. Burning velocity S_b as a function of time. Top light blue curve: adiabatic; bottom orange curve: observed S_b with OTM radiation; middle curves: corrected S_b, red broken line via (Eq. (7)), and dark blue line, (Eq. (10)). Note, the two latter curves must be exactly the same and both are shown only as confirmation.

An error is introduced when an extrapolation fit equation (e.g. Eqs. (5) or (6)) is applied to the corrected $R_{f,OTM_{corr}}(t)$ trace. The implied stretch rate is nominally calculated by the corrected flame radius, but the physical correct stretch rate should be $\kappa = 2/R_{f,OTM_{obs}} * \mathrm{d}R_{f,OTM_{obs}}/\mathrm{d}t$, by using the observed flame trace. To quantify the resulting error in the zero-stretch burning velocity, the linear extrapolation Eq. (3) is applied to both traces, the observed and the corrected. Note, as mentioned above this can only be done for the linear extrapolation. For a range of ϕ*'s*, Fig. 6 shows the relative errors of the extrapolated S_b^0. The errors are negligible small, below 1%, for all ϕ*'s*.

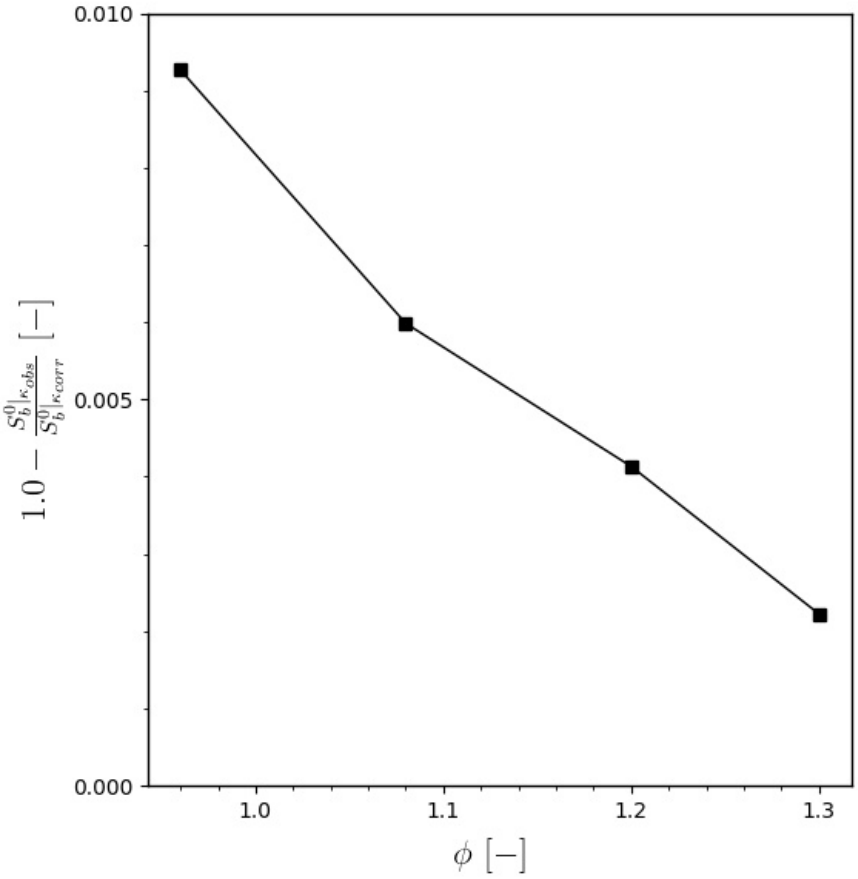

Fig. 6. Relative error in S_b^0 when stretch κ is derived from the corrected flame trace $R_{f,OTM_{corr}}(t)$ instead of $R_{f,OTM_{obs}}(t)$.

4. Results

The numerical simulations are used to generate synthetic radii vs. time data. These data are used for two purposes: 1) to compare with experimental R_f vs t data for model validation, and 2) to explore the data analysis methods using data not affected by optical noise, domain limitations, buoyancy, and potential transition to cellular flame structure. Hence, the numerical R_f vs t data are used to explore the influence of stretch, radiation, and maximum flame diameter (all of which are modeled by the simulations) on the data analysis. Following that, the same methods are applied to the experimental data.

4.1. Calculated Flames

4.1.1. Initial Conditions

The temperature and pressure in the simulations are those of the experiments (101 kPa and 294 K), as are the gas composition, for $\phi = 0.96, 1.08, 1.2,$ and 1.3. The present experiments are limited in domain to about 3 cm diameter, the useful domain being determined by ignition

disturbances, confinement effects and restricted visual access. The simulations, however, are carried out to larger radii, 10 cm, at which stretch effects are smaller and radiation effects larger. The present simulations are initiated by a hot kernel at chemical equilibrium with a radius of 0.5 cm. To exclude ignition effects, data obtained for radii smaller than $R_f = 1\ cm$ are excluded from the analysis. In the following investigations, three different radius ranges are considered: 1) $1\ cm < R_f < 3\ cm$, 2) $1\ cm < R_f < 10\ cm$, and 3) $2\ cm < R_f < 10\ cm$. The first is chosen because (as we will see later) this is about the data range available in experiments, the second represents the maximum range of data available from the simulations, and the third considers only larger radii for which stretch effects on the flame velocity become more linear.

4.1.2. Zero Stretch Extrapolation

For adiabatic conditions, Fig. 7 shows the burned gas velocity S_b as a function of flame stretch κ; and each frame shows the results for one value of ϕ (0.96, 1.08, 1.2, and 1.3), corresponding to the conditions of the experimental runs. Each frame depicts raw traces from the simulations (symbols) and the linear and non-linear fitting lines (from post-processing the data as though it were obtained from experiments). The three dotted lines correspond to linear fits, and the three dashed lines to the non-linear fits. Major observations are that the dependency of burning velocity on stretch rate is increasing with leaner mixtures, the functional dependency is closer to linear for richer mixtures and for lower stretch rates (for all equivalence ratios). As described in Kelley et al. [47], the linear extrapolation always results in larger extrapolated zero stretch values S_b^0. If non-linear data are included, e.g. for $\phi = 0.96$ or 1.08) and the smallest data range applied (range 1, red symbols and lines), the linear extrapolation results in large errors. In contrast, if the data are close to linear, both extrapolation methods give similar results. Ideally, to obtain the most reliable results, one would exclude all non-linear data before the extrapolation procedure is applied, however, as we will see later this is usually not possible when evaluating experimental data.

Similar plots as in Fig. 8 are shown in Fig. 9 for simulations employing the OTM radiation model. Note, that in Fig. 9 the data are corrected for the burned gas velocity, i.e. $S_b = S_{b,OTM_{corr}}$. The same observations and conclusions can be made as for the adiabatic case. The flame traces have similar shapes and are just translated to lower burning velocities, which is the result of the 1st order radiation effect: the radiative energy loss from the reaction zone lowers the temperature in the reaction zone, reducing reaction rates.

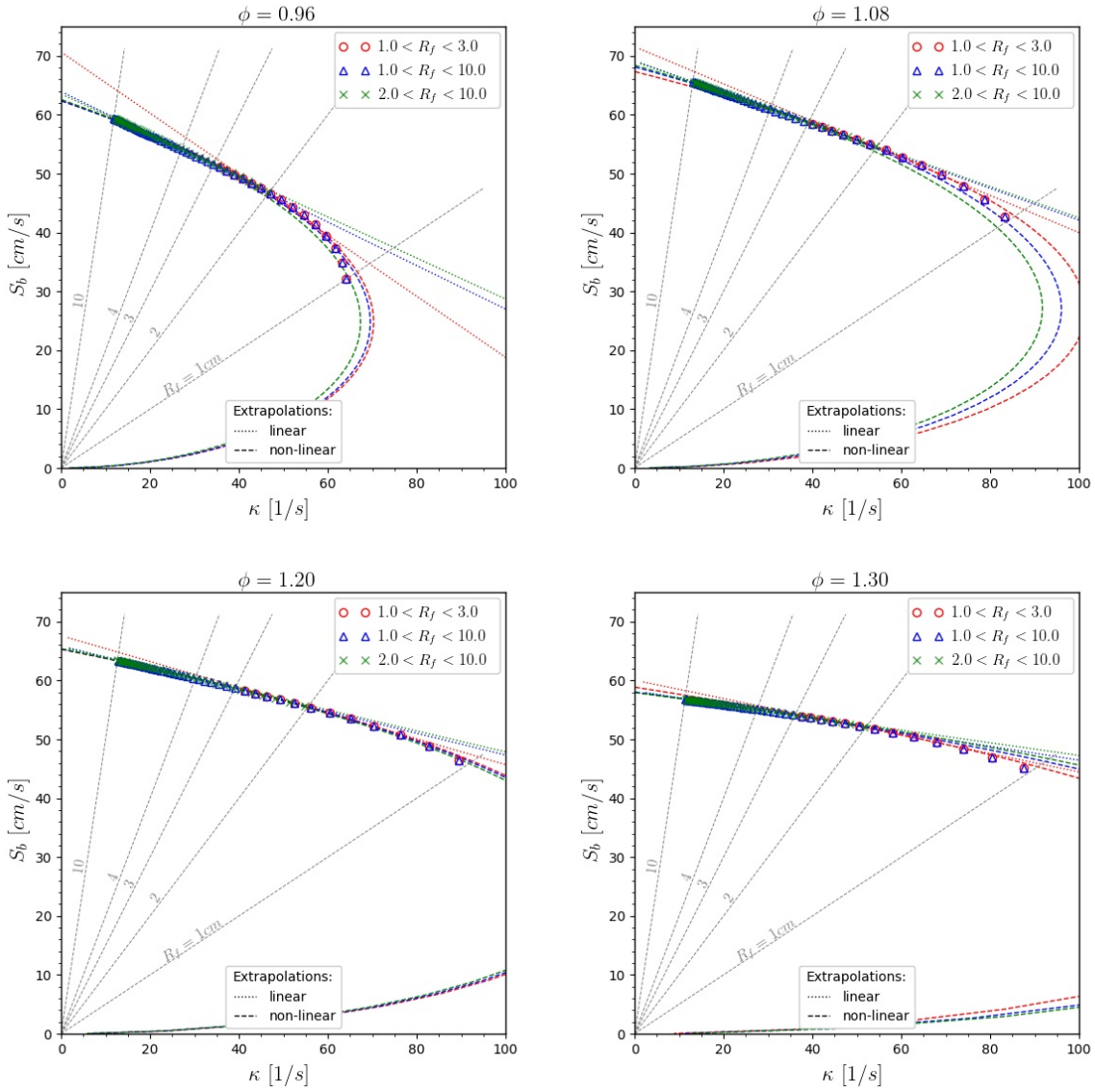

Fig. 7. Raw simulation data (symbols), linear (dotted lines) and non-linear (dashed lines) zero stretch extrapolation for $\phi = 0.96, 1.08, 1.2,$ and 1.3 and for three different data ranges of spherical, adiabatic FlameMaster calculations.

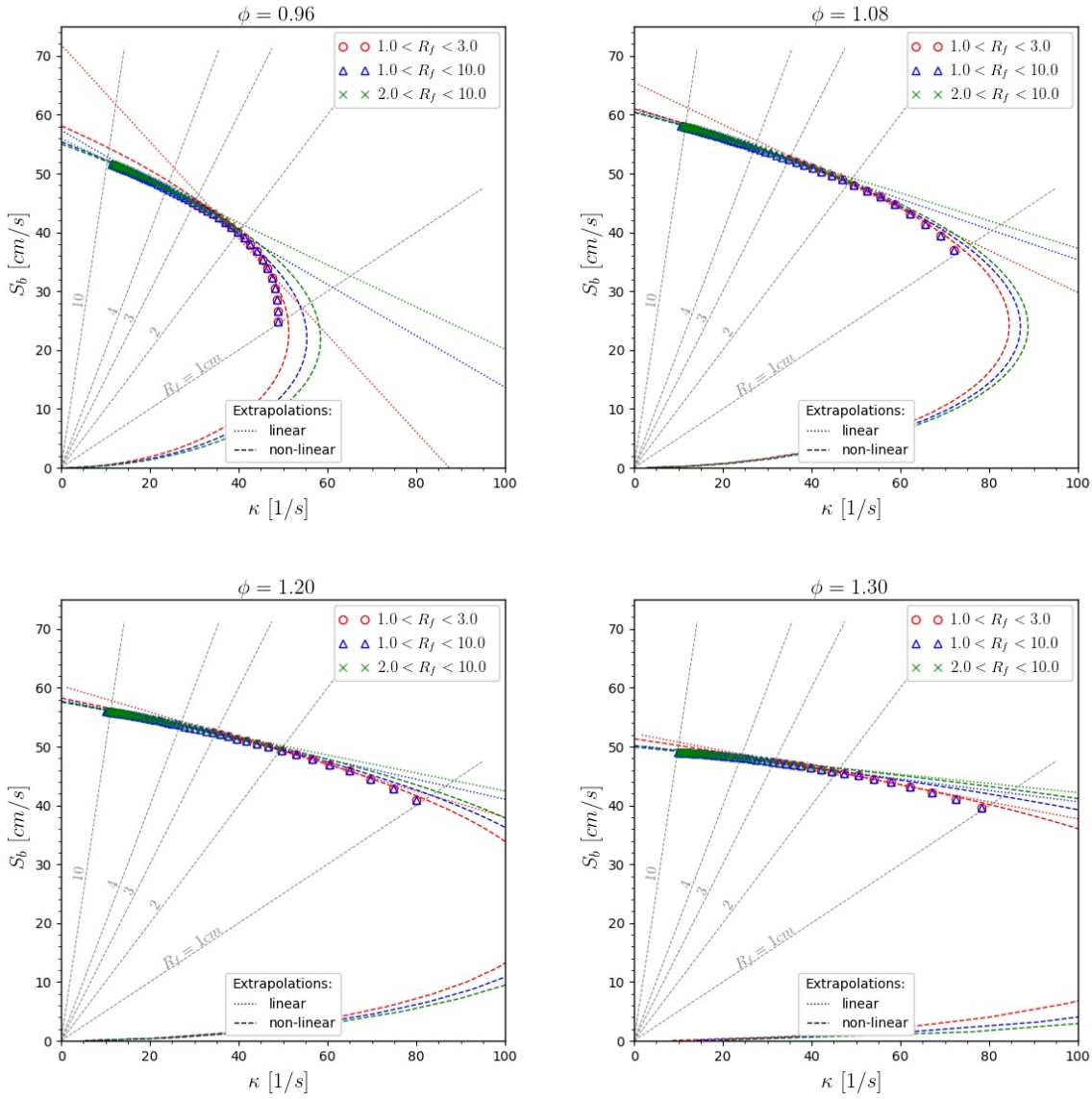

Fig. 8. Raw simulation data (symbols), linear (dotted lines) and non-linear (dashed lines) zero stretch extrapolation for $\phi = 0.96, 1.08, 1.2,$ and 1.3 and for three different data ranges of spherical FlameMaster calculations with the OTM radiation model. The data are corrected for the non-quiescent burned gas velocity.

A completely different picture emerges, as shown in Fig. 9 when using results of the OTM FlameMaster simulations without burned gas correction. Note that these results correspond to what one would observe in the experiments. For each frame in Fig. 9, as the radius increases, the effect of the burned gas velocity becomes larger; i.e. $u_b \propto R_f$. As described by Yu et al. [49] the burned gas velocity is proportional to the radius change of the burned sphere in time ($u_b \propto \mathrm{d}R_f/\mathrm{d}t$) and the radius change of a sphere is proportional to the ratio of the sphere

volume over its surface. Hence, with OTM radiation, u_b increases for small flame sizes approximately linearly with R_f as the burned gases near the center of the flame cool down. For small flame radii, the results for corrected and uncorrected S_b (e.g., $S_b(\kappa)$ in Fig. 8 and Fig. 9) are similar, because the burned gas velocity is low. At larger R_f, the deviation becomes apparent. This is the same behavior illustrated in Fig. 5 for $S_b(t)$. In Fig. 9, with decreasing stretch κ, S_b is not linearly increasing with κ, but rather reaches a maximum and then decreases. Interpretation and implications of these findings are discussed below in the context of the data reduction process of experiments; discussion here is included because the effect is very clear in the simulations (i.e., noise in experimental $R_f(t)$ data create significant scatter in the $\mathrm{d}R_f(t)/\mathrm{d}t$ data). A major point from the present analyses is that attempting to obtain zero-stretch values of S_b becomes problematic when radiation-induced flame contraction is occurring. Least square fitting algorithms often fail to converge, and if they do, they have very large uncertainties on the fit parameters (S_b^0, L_b, and C), which is not surprising since the underlying models upon which the linear and non-linear models are based do not include radiative heat losses. An important observation, however, is that even if only the small range of radii data are used, for which the S_b vs κ curve fit converge, the value of the zero stretch extrapolation does not agree well with the value obtained when S_b is corrected for u_b (as in Fig. 9).

As demonstrated above, the simulations show strong effects of stretch and radiation on the laminar burning velocity of R-32/air flames, with implications for the extrapolation to zero-stretch and adiabatic conditions. Below, the data reduction methods and results of the experimental measurements are presented, and the analyses employed above are applied to the experimental data.

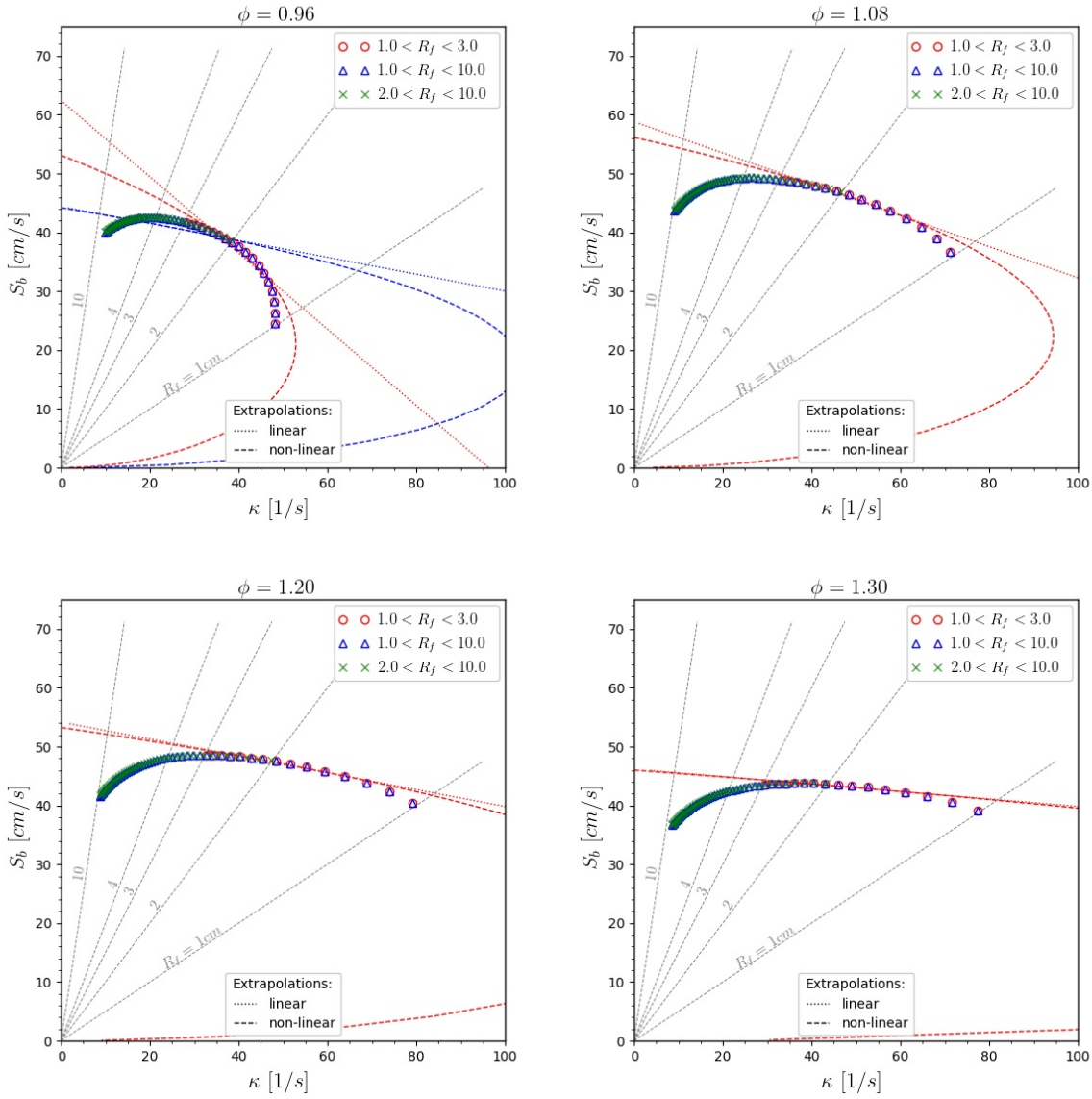

Fig. 9. Raw data (symbols), linear (dotted lines) and non-linear (dashed lines) zero stretch extrapolation for $\phi = 0.96, 1.08, 1.2,$ and 1.3 and for three different data ranges of spherical FlameMaster simulations with the OTM radiation model. The data are not corrected for the non-quiescent burned gas velocity. Note that some extrapolation lines are missing because the least-square fitting algorithm sometimes failed for the radiation-influenced data.

4.2. Experimental Flames

4.2.1. Image Analysis

Fig. 10 and Fig. 11 show shadowgraph images of the time evolution of an R-32/Air flame for equivalence ratios of 1.08 and 0.96, respectively. Two large-scale characteristics can be noted:

1) the flame is moving upwards, and 2) its shape deviates from spherical and becomes toroidal, as described by Berger et al. [31] . These features are more pronounced for low equivalence ratio flames (slower flame velocity). Note that the flame was ignited below the center point of the vessel (and that of the viewing windows) in order to allow more flame images in the circular field of view as the flame moves upwards due to buoyancy.

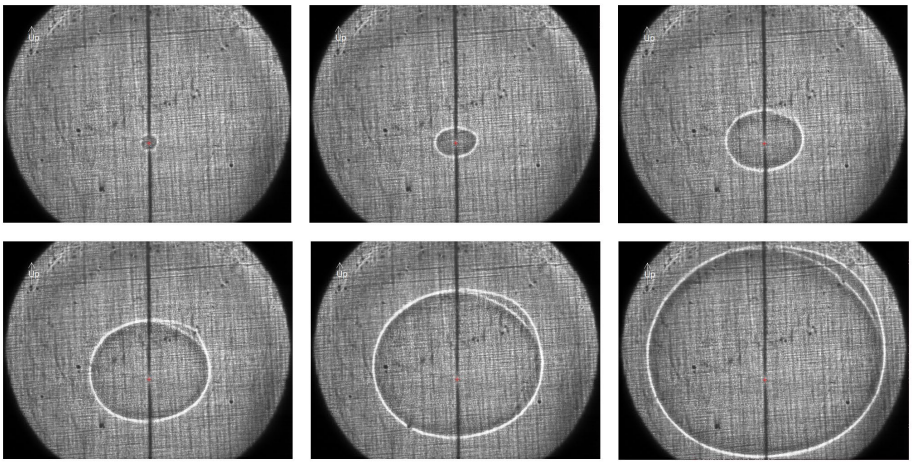

Fig. 10. Shadowgraph pictures of an R-32/Air flame for increasing times and equivalence ratio of 1.08.

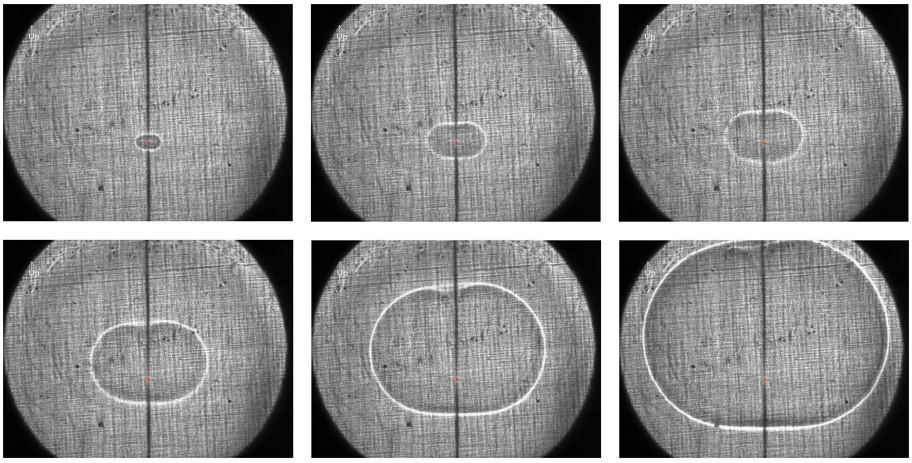

Fig. 11. Shadowgraph pictures of an R-32/Air flame for equivalence ratio 0.96 and increasing time.

To obtain flame velocities from such shadowgraph pictures, representative flame front radius traces of $R_f(t)$ have to be extracted. For flames with little buoyancy (i.e., fast flames), the images have circular cross sections, and any radius is accurate. For slow, buoyant, flames, Pfahl et al. [50] suggested the use of half the horizontal distance d_{hor} between the right and left edges of the flame to represent the flame radius, i.e. $R_f = d_{hor}/2$. This approach is

assumed to reduce the influence of buoyancy, which greatly affects the progression of the top and bottom edges of the flame. This method is one of two approaches adopted in the present work and is referred to as the "edge" or $d_{hor}/2$ method. Under the influence of buoyancy, however, a toroidal vortex forms, creating a dimple in the bottom, and pushing the bottom upward and the left and right edges outward, as discussed in recent 2D DNS modeling of low burning velocity flames [31]. Thus, the left and right edges would have a $\mathrm{d}R_f/\mathrm{d}t$ which is larger than that present in the absence of the vortex. To correct for the translation of the outer edges due to the vortex flow up the center of the bubble, we propose an analysis method based on finding the local curvature of the outer horizontal regions of the toroid, denoted by R_{curv}. Using a flame image from an R-32/air flame at a time from ignition of 60 ms, Fig. 12 illustrates this approach. The flame edge is found (red dots) based on the radial gradient of intensity change. A circle fitting algorithm is applied to the left and right side of the flame within a wedge-shaped sector on each side, represented by the thin white lines. The fitted circles are denoted by the blue and green circles, having centers indicated by the blue and green crosses. Note that the red cross is the initial center of the circular flame (ignition point), and the locations of the blue and green crosses illustrate the upward and outward translation of the horizontal flame edges. The use of the radii of curvature of the fitted circles to represent the flame radius of the left and right edges gives a more accurate accounting of the $\mathrm{d}R_f/\mathrm{d}t$ for the purpose of finding the burned gas velocity S_b from the flame image, partially accounting for the vortex-induced flow up the center of the toroid. In order to assess the two methods ($d_{hor}/2$ and R_{curv}), comparisons between experimental and FlameMaster-simulated data for $R_f(t)$ and $S_b(\kappa)$are considered.

Note that since the flattened flame resembles a toroid, it has three radii: that of the local curvature of the left and right side (R_L and R_R) and that based on half the horizontal extent $d_{hor}/2$. Thus, the local curvature C is (for the right side)

$$C_R = \frac{1}{R_R} + \frac{1}{d_{hor}/2} \tag{12}$$

and the local stretch for the right side κ_R is estimated as

$$\kappa_R = C_R \frac{\mathrm{d}R_R(t)}{\mathrm{d}t} \tag{13}$$

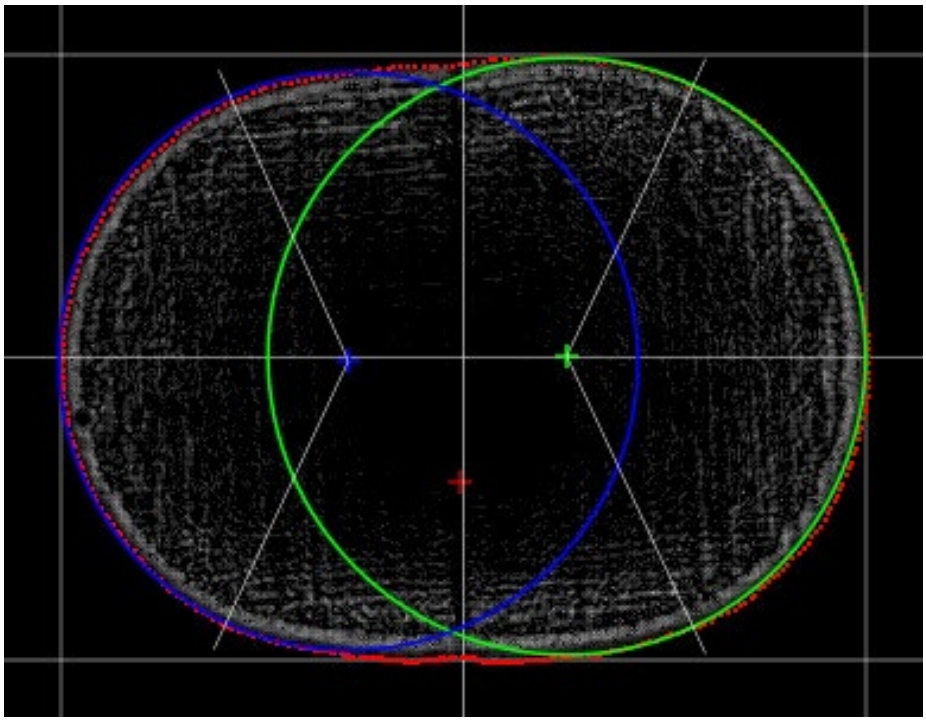

Fig. 12. Illustration of flame front trace extraction methods. White points: shadowgraph image intensity; red points: detected flame front location; vertical thin white lines: edge method flame location based on right and the left outermost extent of flame ($R_f = d_{hor}/2$); blue and green circles: circle-fitting results for left and right side of the flame, through red points within indicated wedge-shaped domain.

4.2.2. Flame Radius vs. Time

Figure 13 shows experimental data as well as simulation results for R_f vs. t, for values of ϕ of 0.96, 1.08, 1.2, and 1.3. In this figure (and Fig. 14, Fig. 16 and Fig. 17), the simulation results are given by the light-blue, orange, and dark-blue lines, for adiabatic, OTM corrected, and OTM observed treatment, respectively (see Section 3.2.5.). In Fig. 13, the red and green curves give the raw experimental data extracted from the video images by using the edge and curvature methods, respectively. For each value of ϕ, each data reduction approach has four experimental curves: two runs for each ϕ, and a left/right side of the flame for each run, except for ϕ=1.3, which has only one run (two curves). All these traces are raw data without smoothing or interpolation. Fig. 13 shows that the raw $R_f(t)$ curves (within each set of red or green curves) are very close to each other, except for one run at $\phi = 0.96$, for which the ignition process was asymmetrical, giving different flame propagation on the left and right sides at early times. Also, comparing the experimental (red/green curves) and the simulations (light blue/blue/orange curves), the early-time data just after ignition shows a much faster growth in $R_f(t)$ in the experiments than in the simulations. This is likely due to the over-driven ignition, necessary for flame propagation in these flames with strong Lewis number effects and having a critical ignition energy to get past the tendency to extinguish at high stretch (low

radius), as has been discussed in the literature [51, 52]. Moreover, it is known that the actual ignition process occurring in the experiments is only treated approximately in the simulations. Hence, to overcome the inaccuracies in modeling the ignition, it is more appropriate to compare the growth of the radius after the flames have grown to a certain size after which the ignition effects have diminished, as discussed previously in the literature [25, 53-56]. This has been accomplished by starting the radius comparisons after $R_f = 1$ cm, except for the case of $\phi = 0.96$, for which $R_f = 2$ cm is used (due to the much stronger Lewis number effect for this flame, as described below).

The modified traces are depicted in Fig. 14. Once the early-time data (disturbed by the ignition process) are removed, the agreement is excellent, as illustrated by the coincidence of the multiple experimental curves (red or green sets of lines), that are nearly indistinguishable in the figure. As is discussed in more detail below, the experimental traces from both data reduction methods generally agree best with the OTM observed calculation rather than the OTM corrected calculation, and the curvature method produces data that agree better with OTM observed than do those from the edge method. As described above, the observed rather than corrected OTM curves should be compared with the experimental curves since the experimental flame locations are not corrected for radiation-induced flame movement of the burned gases. Note that the $R_f(t)$ predicted by the adiabatic model ADI are much larger than the experimentally measured values (using either the curvature or edge data reduction approaches); also, corrected vs. observed is not relevant to the ADI curves since they are equivalent (i.e., no radiation-induced gas movement).

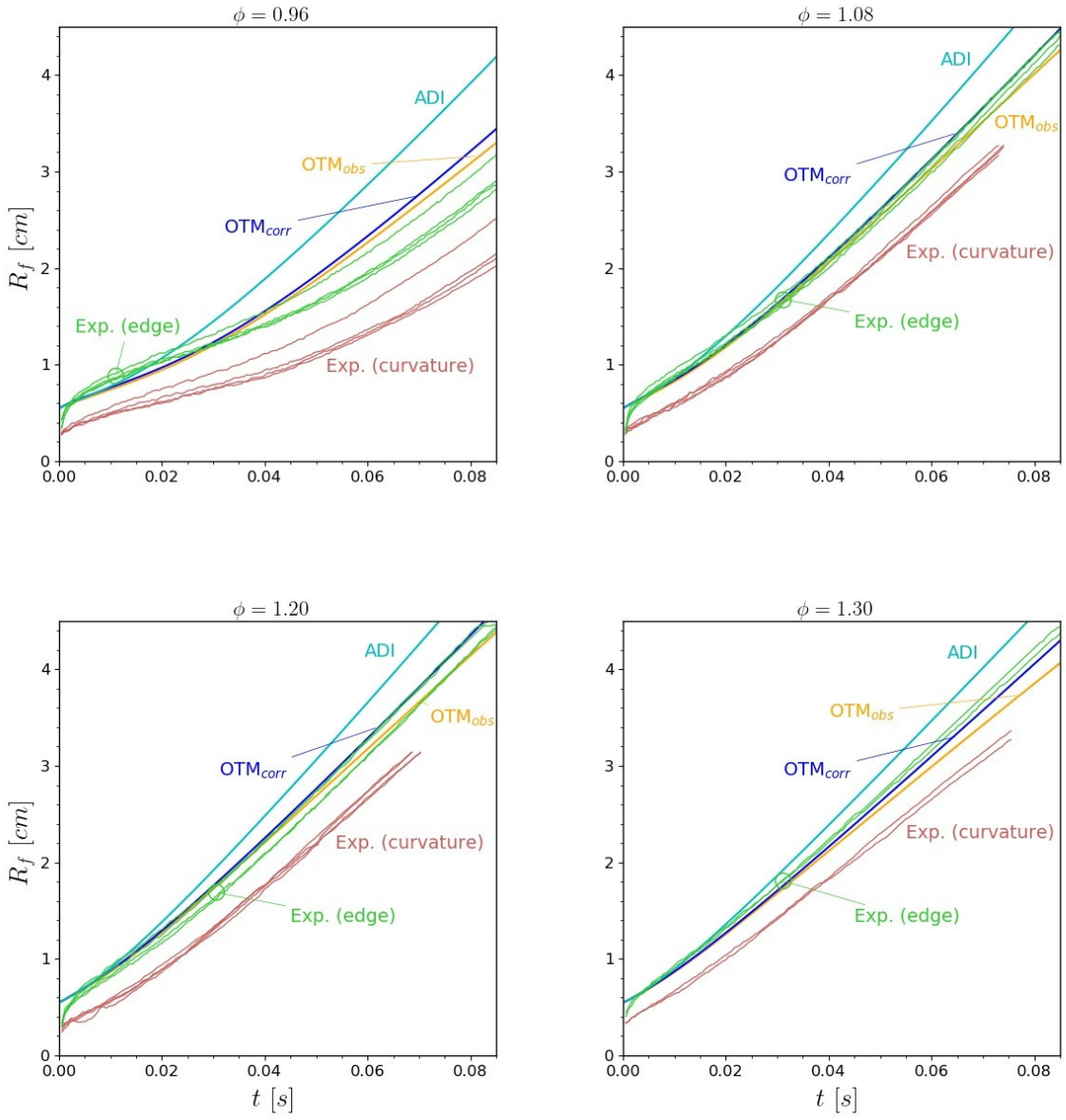

Fig. 13. Raw flame traces $R_f(t)$ for experiments and simulations of different equivalence ratios. The thin green and red lines are experimental data, using edge or curvature approaches. Light blue lines are adiabatic calculation, orange lines OTM calculations without burned gas velocity correction (called OTM_{obs}), and dark blue lines OTM calculation corrected for burned gas velocity (called OTM_{corr}).

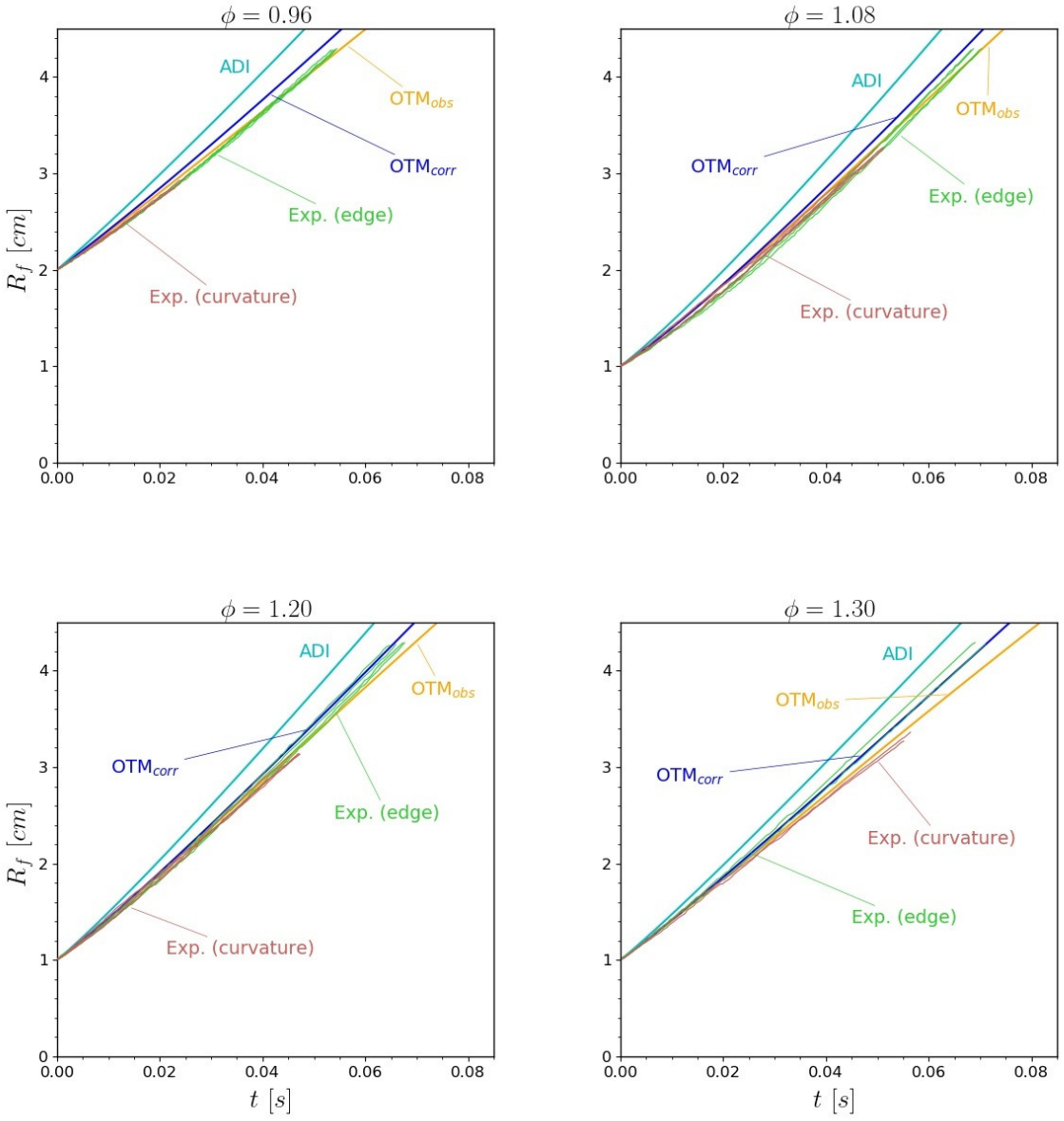

Fig. 14. Similar flame traces of experiments and calculations as in Fig. 13, but translated in time so that $R_f(t)$ all start at the same initial radius at $t = 0$; i.e., after ignition disturbances have died out.

4.2.3. Flame Velocity vs. Radius

A more informative quantity in the context of this work is the flame speed S_b defined as in Eq. (7). In order to simplify the comparison, the multiple experimental flame traces for similar conditions are averaged. For averaging we apply a method similar to the one described by

Lipatnikov et al. [57]. First, similar traces are trimmed in R_f in order to retain only data undisturbed by ignition effects (as in Fig. 14), as has been done previously [25, 53-56]. In the present case the observable radius range is small compared to the size of the vessel, therefore confinement effects are negligible and need not be considered. Edge-extracted flame traces can be tracked to approximately 4.5 cm and curvature-extracted traces up to 3 cm (see Fig. 14). For consistency, these same upper limits on $R_f(t)$ are used for all equivalence ratios; similarly, the same extraction method (edge or curvature) is chosen when averaging $R_f(t)$ data. The trimmed traces span a different range in time, therefore the original time ranges are mapped to the interval [0,1]: $t \rightarrow t'$ with $t \in [0, T_n]$, $t' \in [0, 1]$, T_n is the last time point of trace n. In space t', all traces have the same start and end points and the following averaging method is applied

$$\mathrm{R_{f,ave}(t')} = \frac{1}{\mathrm{N}} \sum_{\mathrm{n=1}}^{\mathrm{N}} R_{f,n}(\mathrm{t'})\,. \tag{14}$$

In which N is the total number of similar traces to average. Finally, t' is mapped backed to the averaged time interval $t \in [0, T]$, with

$$\mathrm{T} = \frac{1}{\mathrm{N}} \sum_{\mathrm{n=1}}^{\mathrm{N}} \mathrm{T_n}\,. \tag{15}$$

Fig. 15 presents, for each value of ϕ, S_b vs. R_f of the averaged experimental $R_f(t)$ traces. Data are shown for extraction of $R_f(t)$ from the flame images using edge (empty symbols) or curvature (filled symbols) extraction methods. Also shown are the calculated OTM observed traces (lines), again for all ϕ (0.96, 1.08, 1.2, and 1.3). In all cases, the curvature-extracted data are much closer to the FlameMaster simulations than are the edge-extracted data. There is generally good agreement between the curvature-extracted experimental data and the simulations, which capture the important features of the flames: variation of S_b with R_f, variation with ϕ (stronger effect for lower ϕ), and stronger variation in S_b with R_f at smaller R_f. These phenomena can be illustrated more clearly via S_b vs. κ plots as described below.

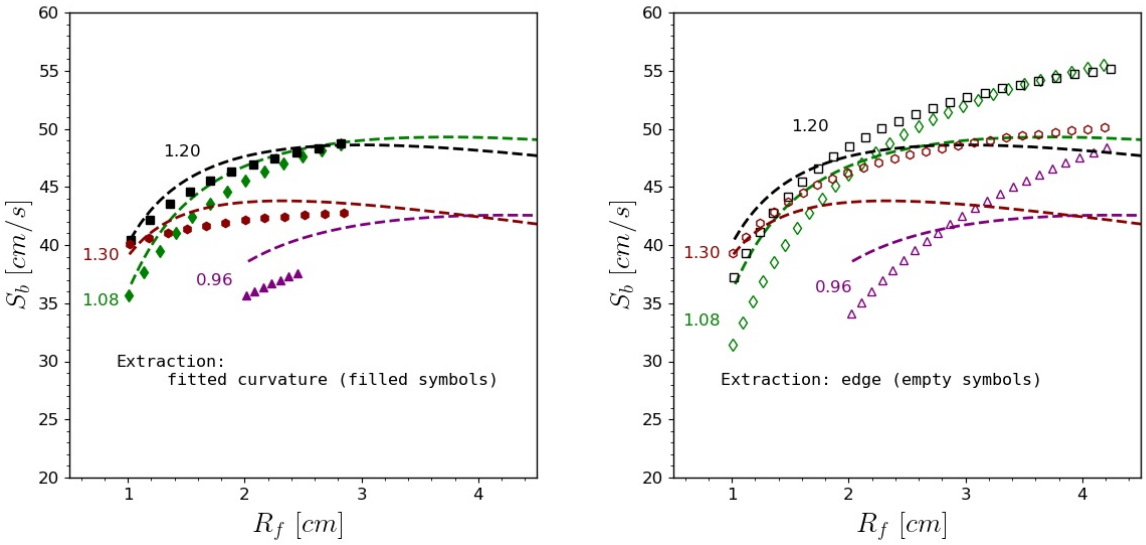

Fig. 15. Experimental edge- (open symbols) and curvature-extracted (filled symbols) and calculated OTM observed (lines) traces for equivalence ratios 0.96, 1.08, 1.2, and 1.3.

4.2.4. Flame Velocity vs. Stretch Rate

4.2.4.1.Averaged Data

Using the $R_f(t)$ and S_b data from Fig. 14 and Fig. 15, Fig. 16 shows S_b as a function of the stretch κ, calculated using Eq. (2). As in Fig. 15, the experimental data are averaged data for each value of ϕ, with one curve each for edge-extracted (green dashed line) or curvature-extracted (red dashed lines) data. For the FlameMaster simulations, there are three curves for S_b as a function of κ: adiabatic (ADI, light blue solid lines), OTM corrected (dark blue lines), and OTM observed (orange lines). The trends are the same as presented above. The adiabatic calculation results in flame velocities well above the experimental values, while the OTM corrected traces have a shape similar to the adiabatic traces but translated to lower values of S_b. The difference in S_b for OTM corrected and ADI shows the radiative first order effect, the direct cooling of the reaction zone. The second order radiation effect, due to the contraction of the burned gases, can be seen by comparing the OTM observed and the OTM corrected traces. For the OTM observed curve, as the stretch rate decreases S_b, instead of continuing to increase, reaches a maximum and then starts to decrease. Thus, the rate of increase in the magnitude of the burned gas velocity (proportional to R_f) is faster than the increase of S_b with decreasing stretch rate. This finding implies that if only experimental data over a limited radius range are available one could conclude that there is little stretch effect, as has been reported for R-32/air flames [13].

Comparing the OTM observed curve with the averaged experimental data (dashed lines), obtained via either the edge- or curvature-extracted data reduction shows that for all values of

ϕ, the curvature method is much closer to the numerical prediction. This is the same result as obtained in the comparisons of the $R_f(t)$ data of Fig. 15; i.e., the curvature extraction is closer to the calculation. Note, that for S_b, it is difficult to compare exactly the evolution of the calculated and averaged experimental traces since during the averaging process, smoothing and interpolation of the raw data are necessary. Nonetheless, the trends in the experimental data (for example the variation of S_b with κ) are captured by the numerical simulation (OTM observed) and imply that the curvature extraction method is superior to the edge method.

For lean flames the experimental uncertainties are larger (see Fig. 16) because: a) the low heat release rate makes the heat loss to the electrodes more important, b) the low burning velocity of these flames makes them more susceptible to buoyancy-induced flame disruptions, and c) at the high-Lewis number of these lean flames, it is known that there exists a critical flame radius below which the flame will not propagate unless it is overdriven in the ignition process [51, 58] . Hence, the poorer agreement for the R-32/air flames with equivalence ratio of 0.96 is expected.

4.2.4.2.Raw Data

In order to explore any potential bias introduced in the averaging of the experimental data, Fig. 17 shows the same data of S_b vs. κ as in Fig. 16 but for all of the non-averaged individual experimental runs plotted together. The raw experimental data are depicted by the red or green symbols, while the averaged experimental data are represented by the red or green dashed lines. Note that there is significant scatter in the data, even though a Savitzky-Golay filter has been applied to the data to bring the scatter to within reason. For all values of ϕ in Fig. 17 (i.e., the individual frames), the curves of the averaged experimental data appear to be reasonable fits to the raw data (points). Hence, based on the non-averaged experimental data, the observations made above are still valid:

1.) The curvature-extracted experimental data match the DNS simulation (OTM observed) better, and the edge-extracted experimental data shows too much variation with stretch compared to any of the simulations (OTM corrected, OTM observed, or ADI).

2.) The S_b obtained by correcting for radiation-induced flame contraction (OTM corrected) yield curves significantly higher and with a different dependence on κ than those obtained while not accounting for flame contraction (OTM observed).

3.) Extrapolations of the S_b vs. κ curves using the OTM corrected vs. OTM observed curves will yield significantly different zero-stretch values of S_b .

Note that while these observations are true for all values of ϕ, the data at $\phi = 0.96$ have significant errors which are expected, as described above.

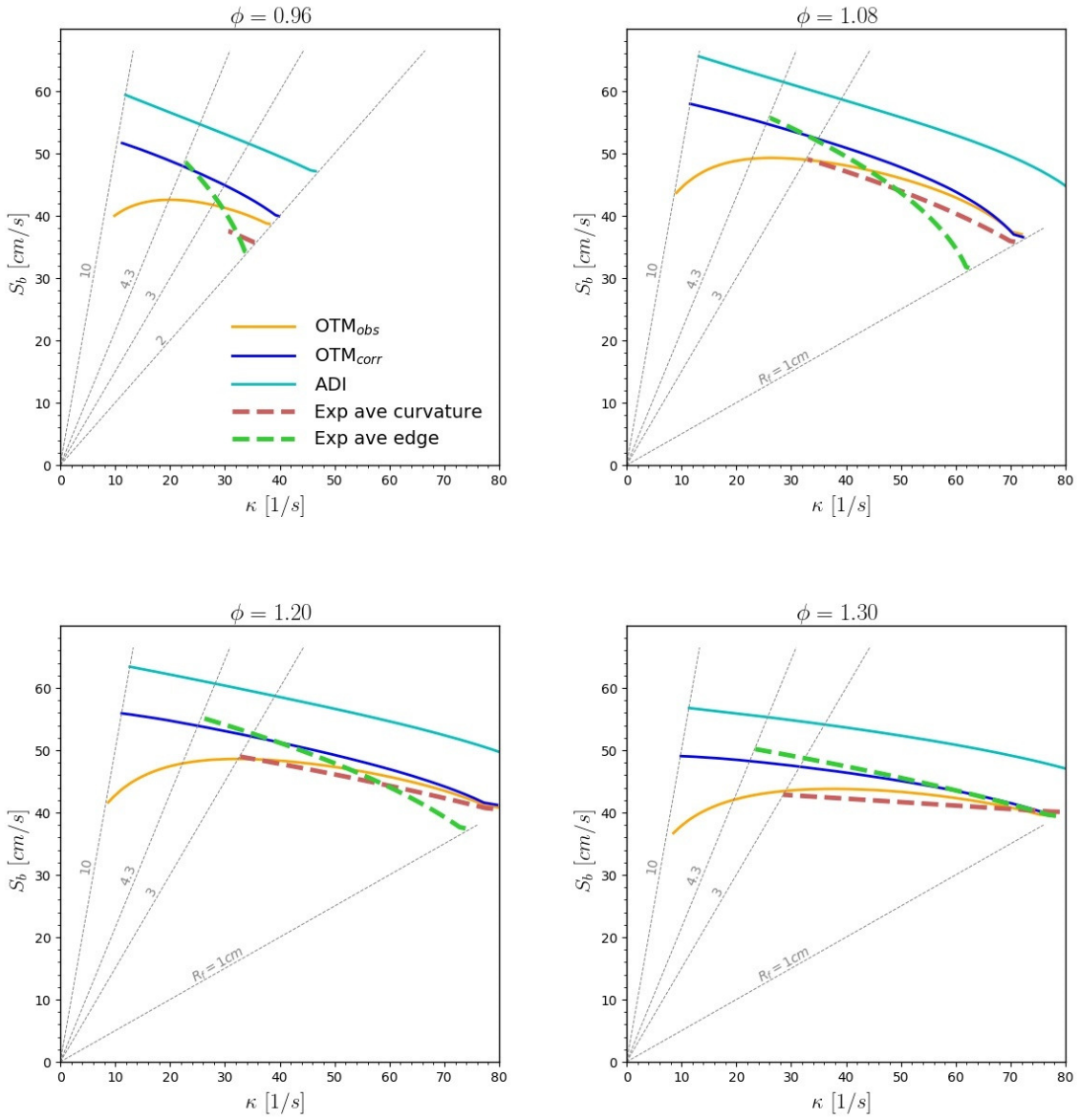

Fig. 16. Calculated and averaged experimental flame traces in $S_b - \kappa$ space for different equivalence ratios. The light blue, the dark blue, and the orange lines show adiabatic, OTM corrected, and OTM observed calculated data, and the broken green and red lines are the averaged experimental results for edge and curvature extraction, respectively.

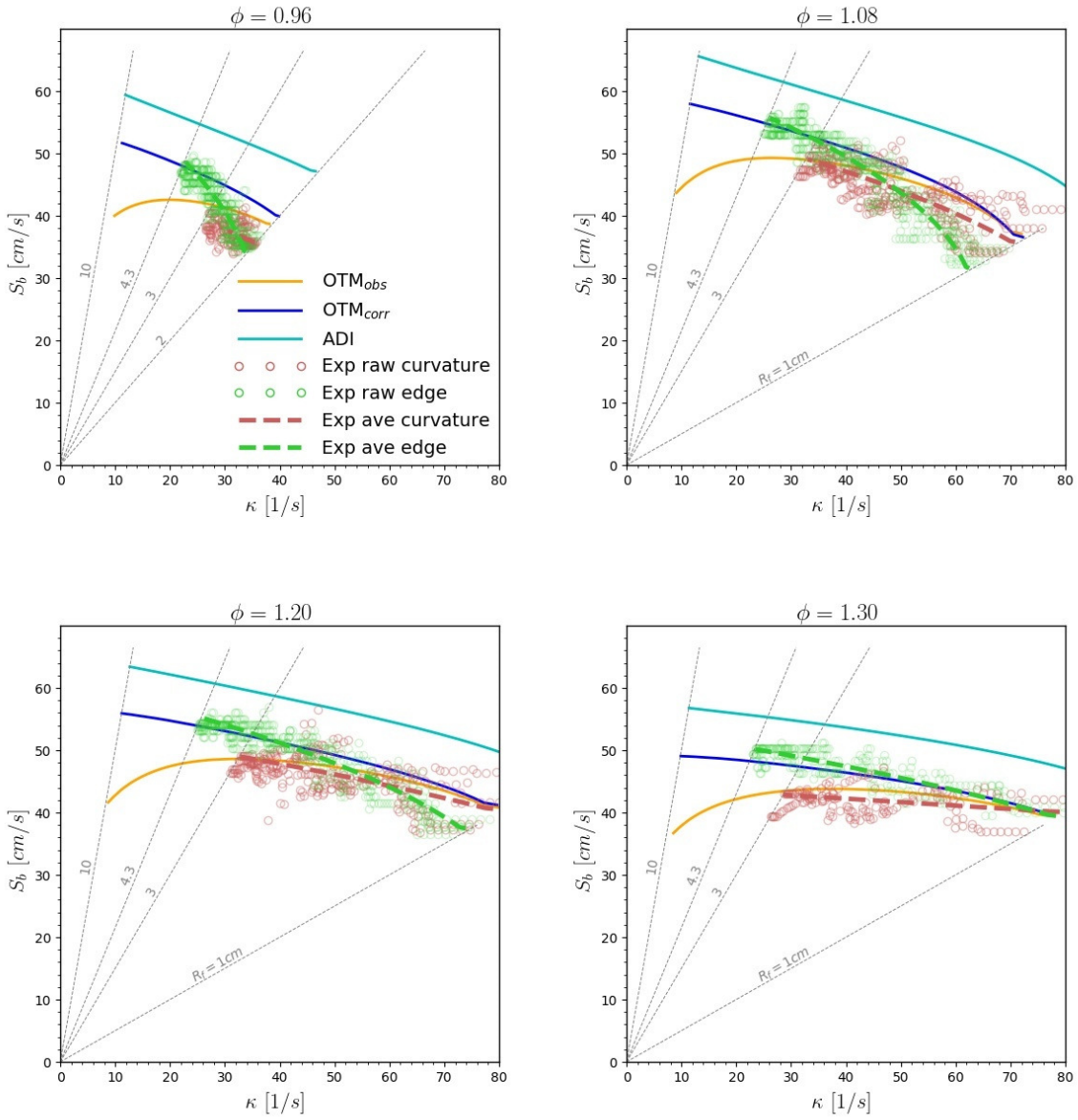

Fig. 17. Experimental (open symbols), averaged experimental (thick dashed lines), and simulated S_b vs κ for different equivalence ratios. Red circles: $R_{f,curv}$, green circles: $d_{hor}/2$. The light blue, the dark blue, and the orange lines show adiabatic, OTM corrected, and OTM observed calculated data.

4.3. Zero Stretch Extrapolation of Experimental Results

Outwardly propagating spherical flames are being used to measure the burning velocity of slow-burning refrigerant-air flames, and typically, unstretched burning velocities are desired.

Two major problems arise when applying standard stretch extrapolation methods to the experimental $S_b - \kappa$ flame traces of refrigerant flames: the limited data window, and the influence of the (unknown) burned gas velocity. Both issues were addressed in section 4.1 on the basis of calculated flame traces. Considering these findings, the conclusion is that currently there is no simple method to reliably extrapolate the observed experimental flame velocity data to zero stretch. Nonetheless, for illustration purposes, it is of interest to compare zero stretch flame velocities between calculations and experiments. In the present analyses, the data window for either experimental data or simulation data, is limited for all considered traces to $1\text{ cm} < R_f < 3\text{ cm}$ for $\phi = 1.08, 1.2, 1.3$ and to $2\text{ cm} < R_f < 3\text{ cm}$ for $\phi = 0.96$. This upper limit corresponds to the shortest of the curvature-extracted traces; a side benefit of this somewhat small upper limit ($R_f = 3$ cm) is that radiation, particularly the burned gas velocity, has less influence for smaller radii. Fig. 18 shows the resulting zero stretch flame velocities obtained from non-linear extrapolation; as explained in section 4.1 for the calculated flames, a linear extrapolation would lead to unrealistic high zero stretch values, and hence are not considered.

The most straightforward extrapolations in Fig. 18 are those from the adiabatic (light blue) and the OTM corrected (dark blue) simulations since the behavior in $S_b - \kappa$ space is close to linear. These curves show that the direct radiation effects lower the flame velocity up 15% for the investigated ϕ-range. Extrapolations for the other traces are questionable for the reasons as described above but are presented nonetheless since they shed light on approaches being used in the literature.

Consistent the with the results described above (see Fig. 15 and Fig. 16), the curvature-extracted zero-stretch burning velocities (red open circles) agree well with the OTM observed values (which are the proper simulation results to be compared to the experimental data), except for the poor agreement for leans flames as discussed. Moreover, the edge-extracted values of S_b^0 (green open circles) are much larger.

Finally, the dashed orange line in Fig. 18 shows the zero-stretch burning velocities obtained if both stretch and radiation are assumed to be negligible, as has been done in earlier work [13]. In this approach the S_b is obtained from the average value over all stretch rates in the data window. This approach gives much lower values of S_b^0, since both the effects of burned gas velocity and stretch are neglected. A conclusion of the present modeling work is that from the experimental data (uncorrected for burned-gas velocity), it might appear that the stretch effect is small. For example in Fig. 16 for $\phi = 1.08$, if one examined S_b (from the OTM observed curved which should represent experimental results) for $2cm < R_f < 4cm$ (a typical range for experimental data), one could conclude that there is little stretch effect (since the effects of stretch and burned gas velocity mostly cancel each other for these conditions). Examination of the ADI and OTM corrected curves in Fig. 16, however, shows that both radiation and stretch are important and significantly raise the S_b^0 if considered, as also shown in Fig. 18. For example, in Fig. 18, the peak of the unstretched adiabatic burning velocity (ADI curve) is almost 50 % higher than the peak of the OTM observed (mean) curve, which is what one would obtain by averaging (over data at all radii) the observed $\mathrm{d}R_f(t)/\mathrm{d}t$ in the laboratory reference frame.

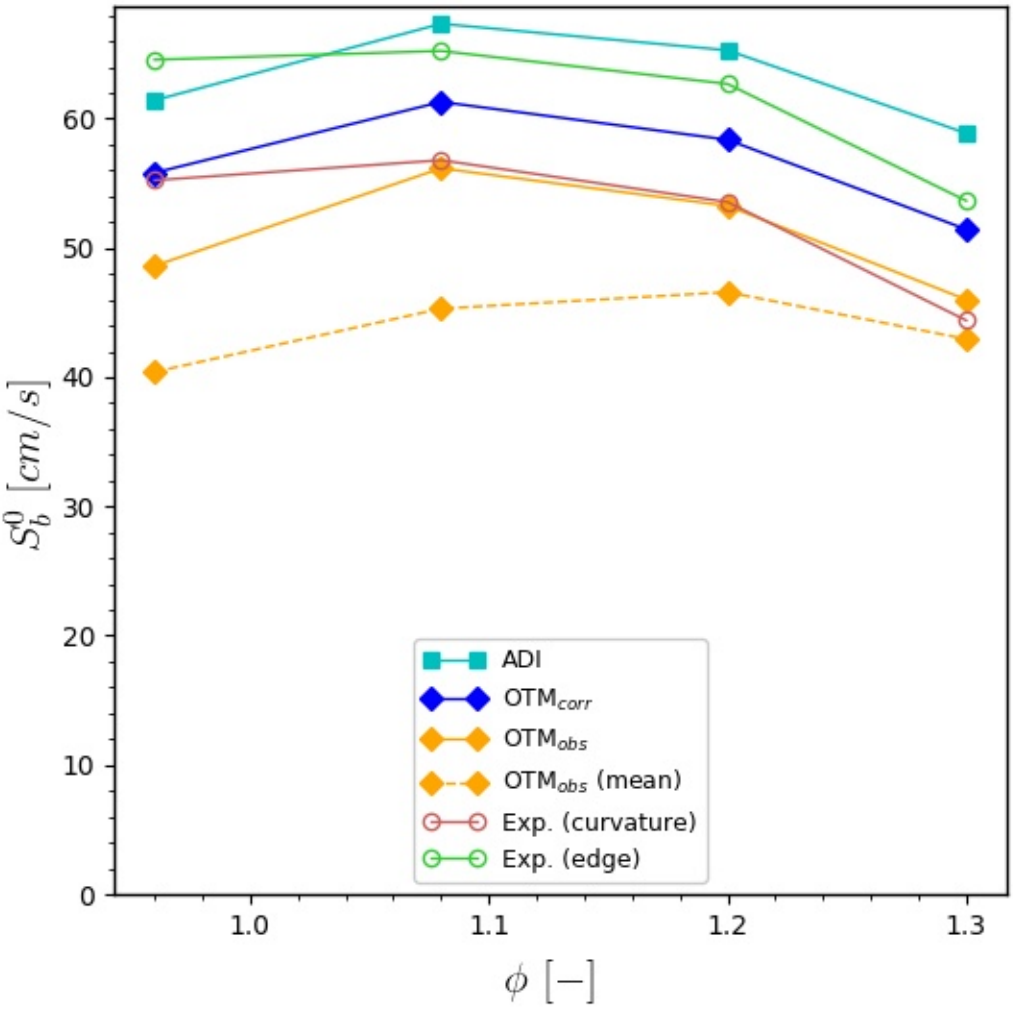

Fig. 18. Extrapolated zero stretch flame velocities S_b^0 derived from adiabatic and OTM calculations and from edge- and curvature-extracted experiments.

5. Conclusions

Calculated and experimentally obtained flame traces of spherically expanding constant pressure R-32/Air flames are analyzed. A method for correcting the flame traces in $R_f - t$ space for the burned gas velocity is presented which allows one to apply the non-linear extrapolation procedure directly on the corrected flame trace. The data reduction process and the issues arising are explained via simulations employing adiabatic and optically thin models for radiation. Finally, two different methods are studied for finding the flame radius from experimental flame images.

Radiation and stretch rate effects play a major role for slow burning R-32/Air flames and prevent the application of established data reduction processes and zero stretch extrapolations. Furthermore, the influence of buoyancy disturbs the flame evolution and makes the extraction of a representative flame radii challenging.

However, under the assumption that the optically thin radiation model is close to the physically correct behavior the following conclusions can be drawn:

1. The first order (direct) radiation effect decreases the flame velocity by up to 15%.
2. If the indirect radiation effect (burned gas velocity) is not considered the burning velocity is greatly underestimated. By how much depends at which flame radius S_b is considered, or, if comparing S_b^0, how the extrapolation procedure is applied.
3. For comparing calculated with experimental data one should use the OTM observed (no burned gas velocity correction) flame traces.
4. If examining experimental data, the opposing effects of stretch and flame contraction due to radiative heat loss on $\mathrm{d}R_f/\mathrm{d}t$ with decreasing stretch rate (increasing flame radius) can lead to the partial cancelling of their effects, and therefore to the incorrect conclusion that there are no stretch or radiation effects on the burning velocity.
5. Extracting experimental flame traces by considering the left and right horizontal flame edges (edge method) yields zero stretch flame velocities that are significantly higher than those obtained by tracking the flame curvature (which account for the translation of the flame edges due to upward vortex-induced flow up the center). Therefore, it can be concluded that the edge-tracking method overestimates the burning velocities.
6. Fitting circles to the left and right flame edges and using the circle radii as the representative flame traces $R_f(t)$ yields zero stretch burning velocities which are similar to the OTM observed calculation.

Acknowledgements

The authors would like to thank Dr. Kenji Takizawa and Prof. Li Qiao for input concerning their experimental setups, upon which ours was based. Thomas Mullins, Cedric DeBelle, and Robert Morrison wrote the image analysis program. This work was supported by the Buildings Technologies Office of the U.S. Department of Energy, Office of Energy Efficiency and Renewable Energy under contract no. DE-EE0007615 with Antonio Bouza serving as Project Manager.

References

[1] Anonymous The Montreal Protocol on Substances that Deplete the Ozone Layer as Adjusted and/or Amended in London 1990, Copenhagen 1992, Vienna 1995, Montreal 1997, Beijing 1999.

[2] Velders GJ, Ravishankara AR, Miller MK, Molina MJ, Alcamo J, Daniel JS, Fahey DW, Montzka SA, Reimann S (2012) Preserving Montreal Protocol climate benefits by limiting HFCs. *Science* 335(6071):922-923.

[3] Peters N (2000) *Turbulent Combustion* (Cambridge University Press, Cambridge).

[4] Hansen OR, Hinze P, Engel D, Davis S (2010) Using computational fluid dynamics (CFD) for blast wave predictions. *Journal of Loss Prevention in the Process Industries* 23(6):885-906. https://doi.org/10.1016/j.jlp.2010.07.005

[5] Hisken H, Enstad G, Middha P, van Wingerden K (2015) Investigation of concentration effects on the flame acceleration in vented channels. *Journal of Loss Prevention in the Process Industries* 36:447-459.

[6] ASHRAE (2016) ANSI/ASHRAE Standard 34-2016, Designation and Safety Classification of Refrigerants. (American Society of Heating, Refrigerating and Air-Conditioning Engineers, Atlanta, GA).

[7] ISO (2017) International Organization for Standarization (ISO-817): Refrigerants—Designation and safety classification. . (Geneva, Switzerland).

[8] Myhre G, Shindell D, Bréon F-M, Collins W, Fuglestvedt J, Huang J, Koch D, Lamarque J-F, Lee D, Mendoza B (2013) Anthropogenic and natural radiative forcing. *Climate change* 423:658-740.

[9] Myhre G, Shindell D, Breon FM, Collins W, Fuglestvedt JS, Huang J, Lamarque JF, Lee D, Mendoza B, Nakajima T (2014) Anthropogenic and Natural Radiative Forcing. *Climate Change 2013 – The Physical Science Basis: Working Group I Contribution to the Fifth Assessment Report of the Intergovernmental Panel on Climate Change*, ed Intergovernmental Panel on Climate C (Cambridge University Press, Cambridge), pp 659-740.

[10] Burgess Jr DR, Manion JA, Burrell RR, Babushok VI, Hegetschweiler MJ, Linteris GT (2019) A Validated Model for Burning Velocities of R-32/O_2/N_2 Mixtures over a Wide Range of Conditions. *Combust Flame* submitted.

[11] Linteris GT , Truett L (1996) Inhibition of premixed methane-air flames by fluoromethanes. *Combust Flame* 105(1-2):15-27. https://doi.org/Doi 10.1016/0010-2180(95)00152-2

[12] Takizawa K, Takahashi A, Tokuhashi K, Kondo S, Sekiya A (2005) Burning velocity measurement of fluorinated compounds by the spherical-vessel method. *Combust Flame* 141(3):298-307. https://doi.org/DOI 10.1016/j.combustflame.2005.01.009

[13] Takizawa K, Takagi S, Tokuhashi K, Kondo S, Mamiya M, Nagai H (2013) Assessment of Burning Velocity Test Methods for Mildly Flammable Refrigerants, Part 1: Closed-Vessel Method. *ASHRAE Trans* 119(2):243-254.

[14] Moghaddas A, Bennett C, Rokni E, Metghalchi H (2014) Laminar burning speeds and flame structures of mixtures of difluoromethane (HFC-32) and 1,1-difluoroethane (HFC-152a) with air at elevated temperatures and pressures. *HVAC&R Research* 20(1):42-50. https://doi.org/10.1080/10789669.2013.822252

[15] Burrell R, Pagliaro JL, Linteris GT (2019) Effects of stretch and thermal radiation on difluoromethane-air burning velocity measurements in constant volume spherically expanding flames. *Proc Combust Inst* 37(3):4231-4238. https://doi.org/https://doi.org/10.1016/j.proci.2018.06.018

[16] Burgess DR, Manion JA, Burrell RR, Babushok VI, Hegetschweiler MJ, Linteris GT (2019) Validated Model for Burning Velocities of R-32/O_2/N_2 Mixtures over a Wide Range of Conditions. *11th U S National Combustion Meeting, March 24, 2019 - March 27, 2019*, (The Combustion Institute, Pasadena, CA, United states).

[17] Jabbour T (2004) Flammable Refrigerant Classification Based on the Burning Velocity, Ph.D. Thesis. (Ecole des Mines de Paris, Paris France).

[18] Clodic D , Jabbour T (2011) Method of test for burning velocity measurement of flammable gases and results. *HVAC&R Research* 17(1):51-75.

[19] Papas P, Zhang S, Kim W, Zeppieri SP, Colket MB, Verma P (2017) Laminar flame speeds of 2,3,3,3-tetrafluoropropene mixtures. *Proc Combust Inst* 36:1145-1154. https://doi.org/http://dx.doi.org/10.1016/j.proci.2016.06.073

[20] Takizawa K, Igarashi N, Tokuhashi K, Kondo S, Mamiya M, Nagai H, Ashrae (2013) Assessment of Burning Velocity Test Methods for Mildly Flammable Refrigerants, Part 2: Vertical-Tube Method. *Ashrae Transactions 2013, Vol 119, Pt 2,* ASHRAE Transactions), Vol. 119, pp 255-264.

[21] Nyden MR, Linteris GT, Burgess DRF, Westmoreland PR, Tsang W, Zachariah MR (1994) Evaluation of Alternative In-Flight Fire Suppressants for Full-Scale Testing in Simulated Aircraft Engine Nacelles and Dry Bays. (Gaithersburg MD), NIST SP 861, 1994.

[22] Burgess Jr DR, Zachariah MR, Tsang W, Westmoreland PR (1995) Thermochemical and chemical kinetic data for fluorinated hydrocarbons. *Prog Energy Combust Sci* 21(6):453-529. https://doi.org/10.1016/0360-1285(95)00009-7

[23] Burgess Jr DR, Zachariah MR, Tsang W, Westmoreland PR (1995) Thermochemical and Chemical Kinetic Data for Fluorinated Hydrocarbons. (National Institute of Standards and Technology, Gaithersburg, MD), NIST Technical Note 1412.

[24] Linteris GT , Babushok VI (2020) Laminar burning velocity predictions for C_1 and C_2 hydrofluorocarbon refrigerants with air. *J Fluorine Chem* 230. https://doi.org/https://doi.org/10.1016/j.jfluchem.2019.05.002

[25] Chen Z (2015) On the accuracy of laminar flame speeds measured from outwardly propagating spherical flames: Methane/air at normal temperature and pressure. *Combust Flame* 162(6):2442-2453. https://doi.org/http://dx.doi.org/10.1016/j.combustflame.2015.02.012

[26] Xiouris C, Ye T, Jayachandran J, Egolfopoulos FN (2016) Laminar flame speeds under engine-relevant conditions: Uncertainty quantification and minimization in spherically expanding flame experiments. *Combust Flame* 163:270-283. https://doi.org/http://dx.doi.org/10.1016/j.combustflame.2015.10.003

[27] Hegetschweiler MJ, Pagliaro JL, Berger L, Hesse R, Beeckmann J, Pitsch H, Linteris GT (2020) Effects of stretch and radiation on the laminar burning velocity of R-32/Air flames. *Sci Technol Built Environ* accepted(26):599-609.

[28] Takizawa K, Tokuhashi K, Kondo S (2009) Flammability assessment of CH2=CFCF3: Comparison with fluoroalkenes and fluoroalkanes. *Journal of Hazardous Materials* 172(2-3):1329-1338. https://doi.org/10.1016/j.jhazmat.2009.08.001

[29] Takizawa K, Tokuhashi K, Kondo S, Mamiya M, Nagai H (2010) Flammability assessment of CH2=CFCF3 (R-1234yf) and its mixtures with CH2F2 (R-32). *2010 International Symposium on Next-generation Air Conditioning and Refrigeration Technology*, (Tokyo, Japan).

[30] Choi BC, Park JS, Ghoniem AF (2016) Characteristics of outwardly propagating spherical flames of R134a(C2H2F4)/CH4/O-2/N-2 mixtures in a constant volume combustion chamber. *Energy* 95:517-527. https://doi.org/10.1016/j.energy.2015.11.043

[31] Beger L, Hesse R, Kleinheinz K, Attili A, Beeckmann J, Pitsch H (2019) A DNS study of the impact of gravity on spherically expanding premixed flames. *The 9th European Combustion Meeting (ECM 2019)*, (The Combustion Institute, Pittsburg, PA).

[32] Beger L, Hesse R, Kleinheinz K, Hegetschweiler MJ, Attili A, Beeckmann J, Linteris GT, Pitsch H (2020) A DNS study of the impact of gravity on spherically expanding premixed flames. *Combust Flame* accepted.

[33] Pagliaro JL, Bouvet N, Linteris GT (2016) Premixed flame inhibition by CF_3Br and $C_3H_2F_3Br$ (2-BTP). *Combust Flame* 169:272-286. https://doi.org/http://dx.doi.org/10.1016/j.combustflame.2016.04.017

[34] Pagliaro JL, Linteris GT, Sunderland PB, Baker PT (2015) Combustion inhibition and enhancement of premixed methane-air flames by halon replacements. *Combust Flame* 162(1):41-49. https://doi.org/10.1016/j.combustflame.2014.07.006

[35] Tseng LK, Ismail MA, Faeth GM (1993) Laminar Burning Velocities and Markstein Numbers of Hydrocarbon/Air Flames. *Combust Flame* 95(4):410-426. https://doi.org/Doi 10.1016/0010-2180(93)90007-P

[36] Kwon S, Tseng LK, Faeth GM (1992) Laminar burning velocities and transition to unstable flames in $H_2/O_2/N_2$ and $C_3H_8/O_2/N_2$ Mixtures. *Combust Flame* 90(3-4):230-246. https://doi.org/Doi 10.1016/0010-2180(92)90085-4

[37] Qiao L, Kim CH, Faeth GM (2005) Suppression effects of diluents on laminar premixed hydrogen/oxygen/nitrogen flames. *Combust Flame* 143(1-2):79-96. https://doi.org/DOI 10.1016/j.combustflame.2005.05.004

[38] Hassan MI, Aung KT, Faeth GM (1998) Measured and predicted properties of laminar premixed methane/air flames at various pressures. *Combust Flame* 115(4):539-550. https://doi.org/Doi 10.1016/S0010-2180(98)00025-X

[39] Pagliaro JL, Linteris GT, Babushok VI (2016) Premixed flame inhibition by $C_2HF_3Cl_2$ and C_2HF_5. *Combust Flame* 163:54-65. https://doi.org/http://dx.doi.org/10.1016/j.combustflame.2015.08.015

[40] Pitsch H (1998) FlameMaster, A C++ Computer Program for 0D Combustion and 1D Laminar Flame Calculations. (RWTH-Aachen University, may be downloaded from https://www.itv.rwth-aachen.de/downloads/flamemaster/).

[41] Bondi S , Jones WP (2002) A combustion model for premixed flames with varying stoichiometry. *Proc Combust Inst* 29(2):2123-2129. https://doi.org/https://doi.org/10.1016/S1540-7489(02)80258-9

[42] Goodwin DG, Moffat HK, Speth RL, Weber BW (2018) Cantera: An object-oriented software toolkit for chemical kinetics, thermodynamics, and transport processes. http:/www.cantera.org, Version 2.4.0. (California Institute of Technology, Pasedena, CA), Vol. 2016.

[43] H.Tien MM (1991) On the Burning Velocity of Stretched Flames. *Combust Flame* (84):238-248.

[44] Williams FA (1975) A review of some theoretical considerations of turbulent flame structure. *AGARD Conference Proceeding, AGARD-CP-164*, (NATO Science and Technology Organization).

[45] Markstein GH (1951) Experimental and Theoretical Studies of Flame-Front Stability. *Journal of the Aeronautical Sciences* 18(3):199-209. https://doi.org/10.2514/8.1900

[46] Matalon M (1983) On Flame Stretch. *Combustion Science and Technology* 31(3-4):169-181. https://doi.org/Doi 10.1080/00102208308923638

[47] Kelley AP, Bechtold JK, Law CK (2011) Premixed flame propagation in a confining vessel with weak pressure rise. *Journal of Fluid Mechanics* 691:26-51. https://doi.org/10.1017/jfm.2011.439

[48] Chen Z (2010) Effects of radiation and compression on propagating spherical flames of methane/air mixtures near the lean flammability limit. *Combust Flame* 157(12):2267-2276. https://doi.org/10.1016/j.combustflame.2010.07.010

[49] Yu H, Han W, Santner J, Gou X, Sohn CH, Ju Y, Chen Z (2014) Radiation-induced uncertainty in laminar flame speed measured from propagating spherical flames. *Combust Flame* 161(11):2815-2824.

[50] Pfahl UJ, Ross MC, Shepherd JE, Pasamehmetoglu KO, Unal C (2000) Flammability limits, ignition energy, and flame speeds in H-2-CH4-NH3-N2O-O-2-N-2 mixtures. *Combust Flame* 123(1-2):140-158.

[51] Chen Z, Burke MP, Ju Y (2011) On the critical flame radius and minimum ignition energy for spherical flame initiation. *Proceedings of the Combustion Institute* 33(1):1219-1226.

[52] Kelley AP , Law CK (2009) Nonlinear effects in the extraction of laminar flame speeds from expanding spherical flames. *Combust Flame* 156(9):1844-1851. https://doi.org/10.1016/j.combustflame.2009.04.004

[53] Bradley D, Gaskell PH, Gu XJ (1996) Burning velocities, Markstein lengths, and flame quenching for spherical methane-air flames: a computational study *Combust Flame* 104:176-198.

[54] Halter F, Tahtouh T, Mounaïm-Rousselle C (2010) Nonlinear effects of stretch on the flame front propagation. *Combust Flame* 157(10):1825-1832. https://doi.org/10.1016/j.combustflame.2010.05.013

[55] Chen Z, Burke MP, Ju Y (2009) Effects of Lewis number and ignition energy on the determination of laminar flame speed using propagating spherical flames. *Proc Combust Inst* 32(1):1253-1260. https://doi.org/10.1016/j.proci.2008.05.060

[56] Chen Z, Burke MP, Ju Y (2009) Effects of compression and stretch on the determination of laminar flame speeds using propagating spherical flames. *Combust Theory and Modelling* 13(2):343-364. https://doi.org/10.1080/13647830802632192

[57] Lipatnikov AN, Shy SS, Li W-y (2015) Experimental assessment of various methods of determination of laminar flame speed in experiments with expanding spherical flames with positive Markstein lengths. *Combust Flame* 162(7):2840-2854. https://doi.org/https://doi.org/10.1016/j.combustflame.2015.04.003

[58] Kelley AP, Jomaas G, Law CK (2009) Critical radius for sustained propagation of spark-ignited spherical flames. *Combust Flame* 156(5):1006-1013.